

# EXPERIMENTAL OBSERVATION OF THE INTERMEDIATE VECTOR BOSONS $W^+$ , $W^-$ and $Z^0$ .

Nobel lecture, 8 December, 1984

by

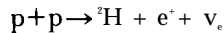
CARLO RUBBIA

CERN, CH-1211 GENEVA 23, Switzerland

## 1. Introduction

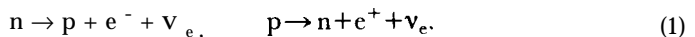
In this lecture I shall describe the discovery of the triplet of elementary particles  $W^+$ ,  $W^-$ , and  $Z^0$  - by far the most massive elementary particles produced with accelerators up to now. They are also believed to be the propagators of the weak interaction phenomena.

On a cosmological scale, weak interactions play an absolutely fundamental role. For example, it is the weak process



that controls the main burning reactions in the sun. The most striking feature of these phenomena is their small rate of occurrence: at the temperature and density at the centre of the sun, this burning process produces a heat release per unit of mass which is only 1/100 that of the natural metabolism of the human body. It is indeed this slowness that makes them so precious, ensuring, for instance, the appropriate thermal conditions that are necessary for life on earth. This property is directly related to the very large mass of the  $W$ -field quanta.

Since the fundamental discoveries of Henri Becquerel and of Pierre and Marie Curie at the end of the last century, a large number of beta-decay phenomena have been observed in nuclei. They all appear to be related to a pair of fundamental reactions involving transformations between protons and neutrons:



Following Fermi [1], these processes can be described perturbatively as a point interaction involving the product of the four participating fields.

High-energy collisions have led to the observation of many hundreds of new hadronic particle states. These new particles, which are generally unstable, appear to be just as fundamental as the neutron and the proton. Most of these new particle states exhibit weak interaction properties which are similar to those of the nucleons. The spectroscopy of these states can be described with the help of fundamental, point-like, spin-1/2 fermions, the quarks, with fractional electric charges  $+2/3e$  and  $-1/3e$  and three different colour states. The universality of the weak phenomena is then well interpreted as a Fermi

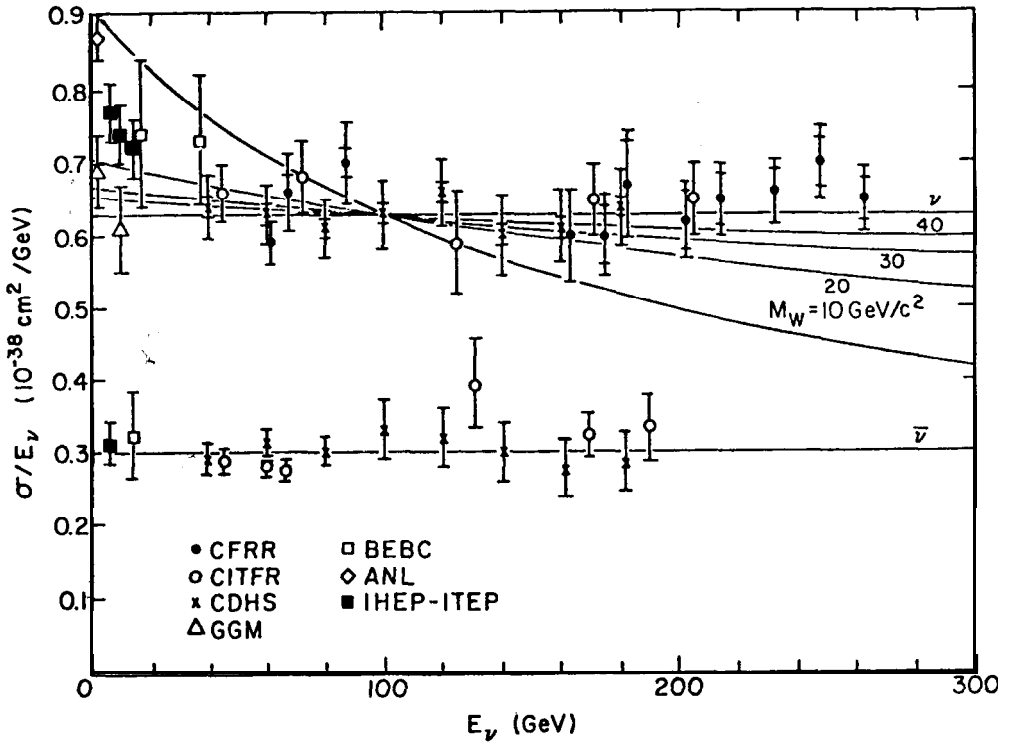


Fig. 1. The muon neutrino and antineutrino charged-current total cross-section as a function of the neutrino energy. Data are from the Particle Data Group (Rev. Mod. Phys. 56, No. 2, Part 2, April 1984) reprinted at CERN. The lines represent the effects of the W propagator.

coupling occurring at the quark level [2]. For instance, reactions (1) are actually due to the processes

$$(d) \rightarrow (u) + e^- + \bar{\nu}_e, \quad (u) \rightarrow (d) + e^+ + \nu_e. \quad (2)$$

where (u) is a  $+2/3e$  quark and (d) a  $-1/3e$  quark. (The brackets indicate that particles are bound.) Cabibbo has shown that universality of the weak coupling to the quark families is well understood, assuming that significant mixing occurs in the  $+1/3e$  quark states [3]. Likewise, the three leptonic families - namely  $(e, \nu_e)$ ,  $(\mu, \nu_\mu)$ , and  $(\tau, \nu_\tau)$  - exhibit identical weak interaction behaviour, once the differences in masses are taken into account. It is not known if, in analogy to the Cabibbo phenomenon, mixing occurs also amongst the neutrino states (neutrino oscillations).

This has led to a very simple perturbative model in which there are three quark currents, built up from the  $(u, d_c)$ ,  $(c, s_c)$ , and  $(t, b_c)$  pairs (the subscript C indicates Cabibbo mixing), and three lepton currents from  $(e, \nu_e)$ ,  $(\mu, \nu_\mu)$ , and  $(\tau, \nu_\tau)$  pairs. Each of these currents has the standard vector form [4]  $J_\mu = f_i \gamma_\mu (1 - \gamma_5) f_j$ . Any of the pair products of currents  $J_\mu, j_\mu$ , will relate to a basic four-fermion interaction occurring at a strength determined by the universal Fermi constant  $G_F$ :

$$\mathcal{L}(x) = (G_F/\sqrt{2}) J_\mu^*(x) j^\mu(x) + \text{c.c.},$$

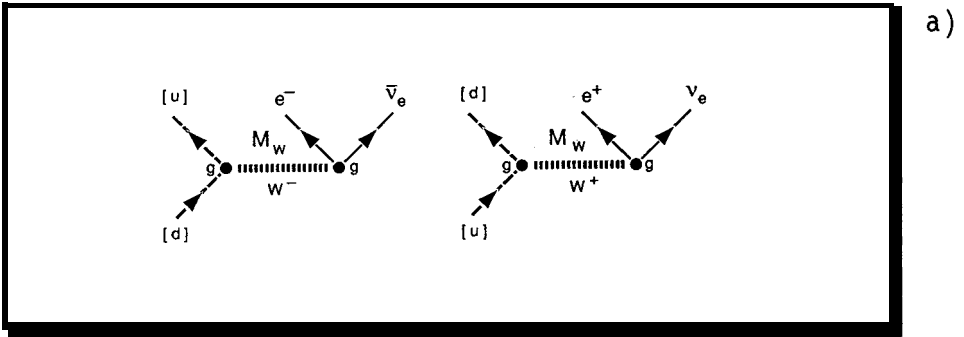


Fig. 2a. Feynman diagram of virtual W exchange mediating the weak process [reaction (2)]

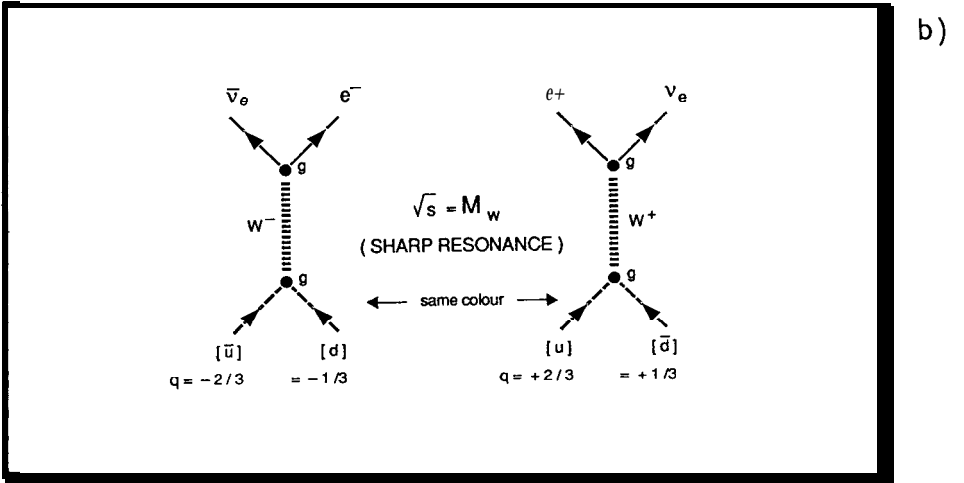


Fig. 2b. Feynman diagram for the direct production of a W particle. Note that the quark transformation has been replaced by a quark-antiquark annihilation.

where  $G_F = 1.16632 \times 10^{-5} \text{ Ge V}^{-2}$  ( $\hbar=c=1$ ).

This perturbative, point-like description of weak processes is in excellent agreement with experiments, up to the highest  $q^2$  experiments performed with the high-energy neutrino beams (Fig. 1). We know, however, that such a perturbative calculation is incomplete and unsatisfactory. According to quantum mechanics, all higher-order terms must also be included: they appear, however, as quadratically divergent. Furthermore, at centre-of-mass energies greater than about 300 GeV, the first-order cross-section violates conservation of probability.

It was Oskar Klein [5] who, in 1938, first suggested that the weak interactions could be mediated by massive, charged fields. Although he made use of Yukawa's idea of constructing a short-range force with the help of massive field quanta, Klein's theory established also a close connection between electromagnetism and weak interactions. We now know that his premonitory vision is embodied in the electroweak theory of Glashow, Weinberg and Salam [6], which will be discussed in detail later in this lecture. It is worth quoting Klein's view directly:

*'The role of these particles, and their properties, being similar to those of the photons, we may perhaps call them "electro-photons" (namely electrically charged photons).'*

In the present lecture I shall follow today's prevalent notation of  $W^+$  and  $W^-$  for these particles-from 'weak' [7] - although one must recognize that Klein's definition is now much more pertinent.

The basic Feynman diagrams of reaction (2) are the ones shown in Fig. 2a.

The new, dimensionless coupling constant  $g$  is then introduced, related to  $G_F/\sqrt{2} \cong g^2/m_W^2$ , for  $q^2 < m_W^2$ . The V-A nature of the Fermi interaction requires that the spin  $J$  of the  $W$  particle be 1. It is worth remarking that in Klein's paper, in analogy to the photon,  $J=1$  and  $g=a$ . The apparently excellent fit of the neutrino data to the four-fermion point-like interaction (Fig. 1) indicates that  $m_W$  is very large ( $\geq 60$  GeV/ $c^2$ ) and is compatible with  $m_W = \infty$ .

## 2. Production of $W$ particles

Direct production of  $W$  particles followed by their decay into the electron-neutrino is shown in Fig. 2b. The centre-of-mass energy in the quark-antiquark collision must be large enough, namely  $\sqrt{s} \cong m_W$ . The cross-section around the resonance will follow a characteristic Breit-Wigner shape, reminiscent of nuclear physics experiments. The cross-section is easily calculated:

$$\sigma(q\bar{q} \rightarrow W) = \frac{3}{4} \pi \lambda^2 \Gamma_i \Gamma_f / [(E - m_W)^2 + \Gamma^2/4],$$

where  $\lambda$  is the reduced quark wavelength in the centre of mass. Quark and antiquark must have identical colours. The initial-state width  $\Gamma_i \equiv \Gamma_{q\bar{q}} \cong 4.5 \times 10^7 \text{ m}^3 (\text{GeV})$  calculated from  $G_F$  is surprisingly wide: namely, for  $m_W \cong 82$  GeV/ $c^2$  as predicted by SU(2) x U(1) theory,  $\Gamma_{q\bar{q}} \cong 450$  MeV. The total width  $\Gamma$  depends on the number of quark and lepton generations. Taking  $N_q=3$  and  $N_l=3$ , again for  $m_W \cong 100$  GeV, we find  $\Gamma = 4 \times \Gamma_{q\bar{q}} = 2$  GeV.

At the peak of the resonance,

$$\sigma(q\bar{q} \rightarrow W, \sqrt{s} = m_W) = 3\pi \lambda_i^2 B_i,$$

where  $B_i = \Gamma_i/\Gamma$  is the branching ratio for the incoming channel.

Of course quark-antiquark collisions cannot be realized directly since free quarks are not available. The closest substitute is to use collisions between protons and antiprotons. The fraction of nucleon momentum carried by the quarks and antiquarks in a proton is shown in Fig. 3. Because of the presence of antiquarks, proton-proton collisions also can be efficiently used to produce  $W$  particles. However, a significantly greater beam energy is needed and there is no way of identifying the directions of the incoming quark and antiquark. As we shall see, this ambiguity will prevent the observation of important asymmetries associated with parity (P) and charge (C) violation of weak interactions. The centre-of-mass energy in the quark-antiquark collision  $s_{q\bar{q}}$  is related to  $S_{p\bar{p}}$  by the well-known formula,

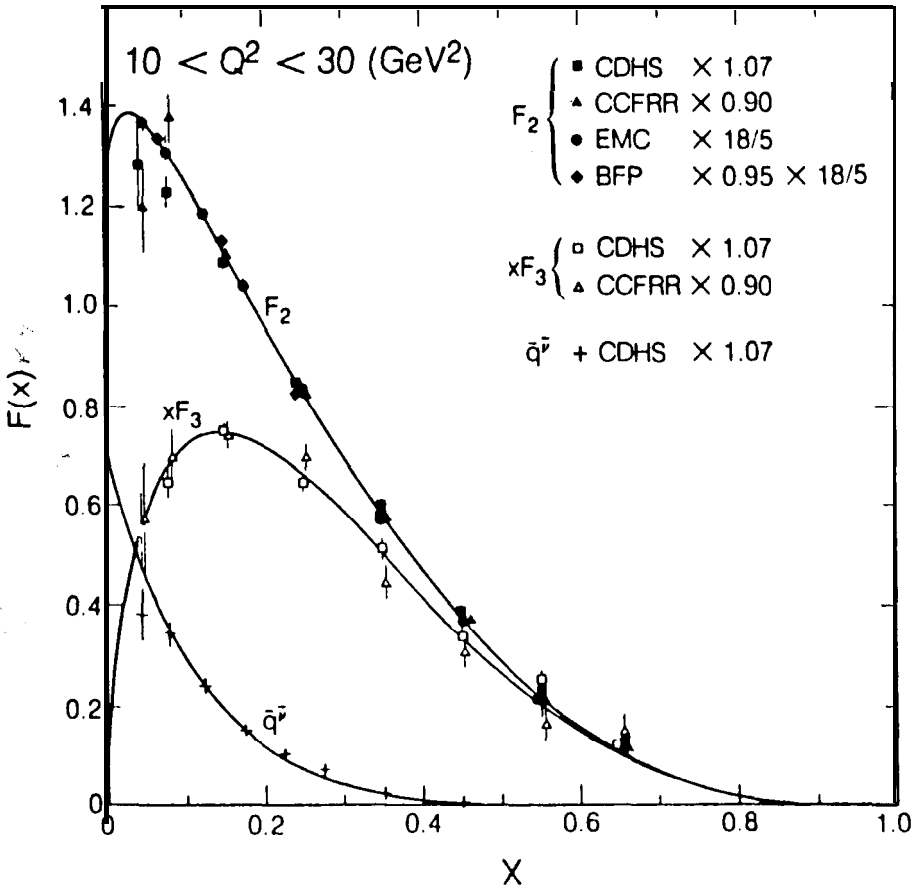


Fig. 3. Structure functions  $F_2$ ,  $xF_3$ , and  $\bar{q}^\nu$ , measured in different experiments, for fixed  $Q^2$  versus  $x$ , plotted assuming  $R = \sigma_T/\sigma_T = 0$ . The electromagnetic structure function  $F_2^{EM}$  measured by the EMC (European Muon Collaboration) and the BFP [Berkeley (LBL) - FNAL- Princeton] is compared with the charged-current structure function  $F_2^{CC}$  using the 18/5 factor from the average charge squared of the quarks. No correction has been applied for the difference between the strange and charm sea quarks, so the interpretation is  $F_2 = x[q + \bar{q} - 3/5(s + \bar{s} - c - \bar{c})]$ . (In this  $Q^2$  range,  $F_2^{EM}$  is depleted by a similar amount due to charm threshold effects in the transition  $s \rightarrow c$ .) The antiquark distribution measured from antineutrino scattering is  $\bar{q}^\nu = x(\bar{u} + \bar{d} + 2\bar{s})$ . The solid lines have the forms:  $F_2 = 3.9x^{0.55}(1-x)^{3.2} + 1.1(1-x)^8$ ,  $xF_3 = 3.6x^{0.55}(1-x)^{3.2}$ ,  $\bar{q}^\nu = 0.7(1-x)^8$ . Relative normalization factors have been fitted to optimize agreement between the different data sets, and absolute changes have been arbitrarily chosen as indicated. [References: CDHS--H. Abramowicz et al., Z. Phys. C17, 283 (1983); CCFRR-F. Sciulli, private communication; EMC-J.J. Aubert et al., Phys. Lett. 105B, 322 (1981); and A. Edwards, private communication; BFP--A. R. Clark et al., Phys. Rev. Lett. 51, 1826 (1983); and P. Meyers, Ph. D. Thesis, LBL-17108 (1983), Univ. of Calif., Berkeley. Courtesy J. Carr, LBL.]

$$s_{q\bar{q}} = S_{p\bar{p}} \cdot x_p \cdot x_{\bar{p}}$$

Note that according to Fig. 3, in order to ensure the correct correlation between the quark of the proton (and the antiquark of the antiproton) the energy should be such that  $x_p \approx x_{\bar{p}} \geq 0.25$ . Therefore there is one broad optimum

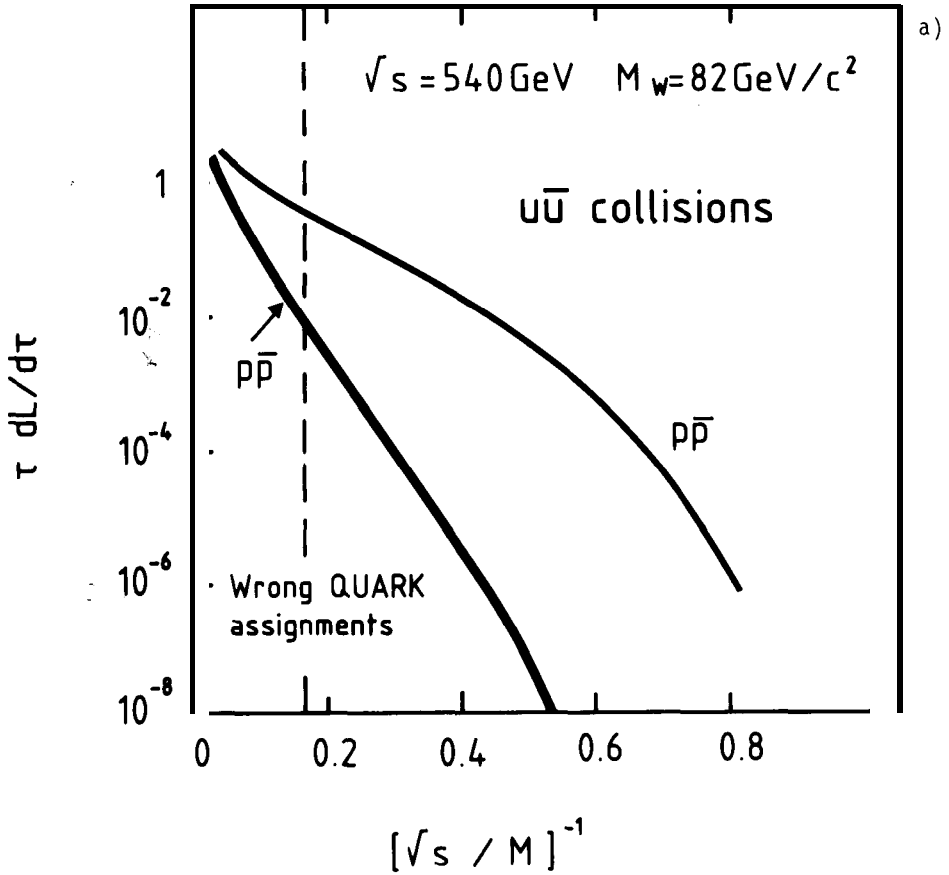


Fig. 4a, b. Production cross-sections of intermediate vector bosons for proton-antiproton collisions. The mass is parametrized with  $\tau^{-1/2} = \sqrt{s}/M$ . Note in Fig. 4a the small probability of wrong quark-antiquark assignments. The prints in Fig. 4b relate to mass predictions for the  $SU(2) \times U(1)$  model.

energy range for the proton-antiproton collisions for a given W mass. For  $m_w = 80 \text{ GeV}/c^2$ ,  $\sqrt{S_{pp}} \approx 400\text{--}600 \text{ GeV}$ . The production cross-section for the process

$$p\bar{p} \rightarrow W^+ X, \quad W^+ \rightarrow e^+ + \nu_e$$

(where X denotes the fragmentation of spectator partons) can be easily evaluated by folding the narrow resonance width over the p and  $\bar{p}$  momentum distributions (Fig. 4). For  $m_w = 82 \text{ GeV}/c$  and  $\sqrt{S_{pp}} = 540 \text{ GeV}$ , one finds  $\sigma \cdot B = 0.54 \times 10^{-33} \text{ cm}^2$ .

### 3. Proton-antiproton collisions

The only practical way of achieving centre-of-mass energies of the order of 500 GeV is to collide beams of protons and antiprotons [8]. For a long time such an idea had been considered as unpractical because of the low density of beams when used as targets.

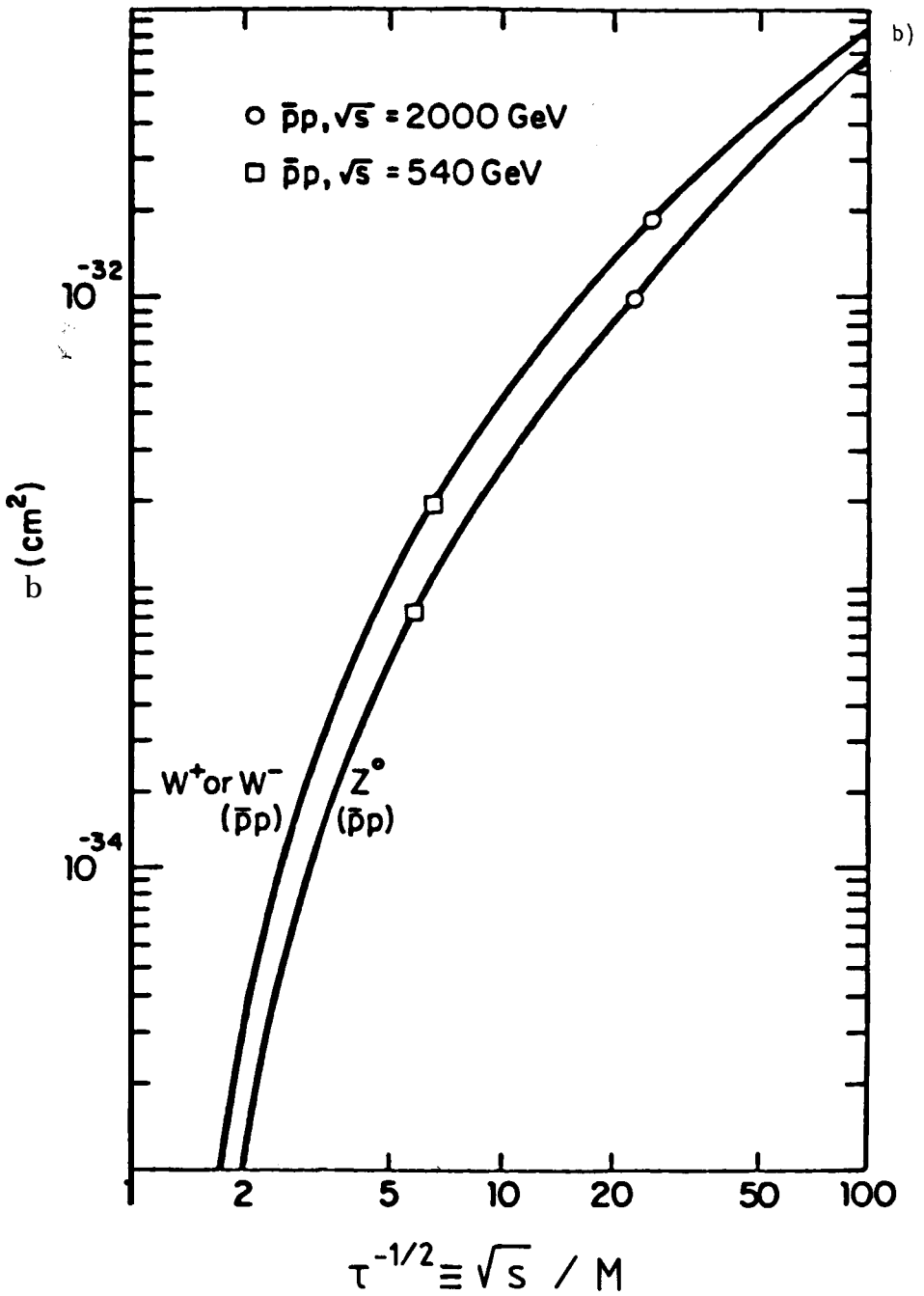


Fig. 4

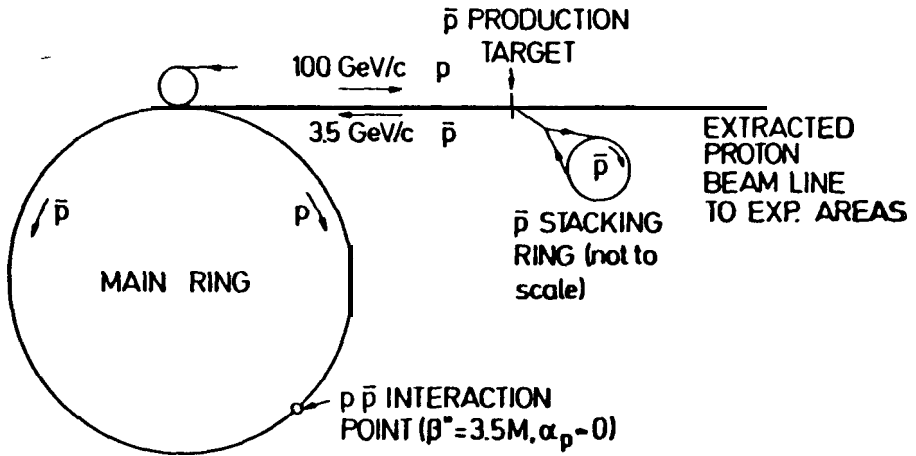


Fig. 5. General layout of the  $p\bar{p}$  colliding scheme, from Ref. [9]. Protons (100 GeV/c) are periodically extracted in short bursts and produce 3.5 GeV/c antiprotons, which are accumulated and cooled in the small stacking ring. Then  $\bar{p}$ 's are reinjected in an RF bucket of the main ring and accelerated to top energy. They collide head on against a bunch filled with protons of equal energy and rotating in the opposite direction.

The rate  $R$  of events of cross-section  $\sigma$  for two counter-rotating beam bunches colliding head on, with frequency  $f_0$  and  $n_1$  and  $n_2$  particles, is

$$R = (n_1 n_2 f_0 / 4) (\sigma / \pi Q^2),$$

where  $Q$  is the (common) beam radius, and the numerical factor 1/4 takes into account the integration over Gaussian profiles. For our experiment, typically  $Q = 0.01$  cm and  $\sigma = 10^{-34}$  cm<sup>2</sup>. Therefore  $(\sigma / \pi Q^2) = 3 \times 10^{-31}$ , and a very large  $n_1 n_2$  product is needed to overcome the 'geometry' effect.

The scheme used in the present experimental programme has been discussed by Rubbia, Cline and McIntyre [9] and is shown in Fig. 5. It makes use of the existing 400 GeV CERN Proton Synchrotron (PS) [10], suitably modified in order to be able to store counter-rotating bunches of protons and antiprotons at an energy of 270 GeV per beam. Antiprotons are produced by collisions of 26 GeV/c protons from the PS onto a solid target. Accumulation in a small 3.5 GeV/c storage ring is followed by stochastic cooling [11] to compress phase space. In Table 1 the parameters of Ref. [9] are given. Taking into account that the original proposal was formulated for another machine, namely the Fermilab synchrotron (Batavia, Ill.) they are quite close to the conditions realised in the SPS conversion. Details of the accumulation of antiprotons are described in the accompanying lecture by Simon van der Meer.

The CERN experiments with proton-antiproton collisions have been the first, and so far the only, example of using a storage ring in which bunched protons and antiprotons collide head on. Although the CERN  $p\bar{p}$  Collider uses *bunched* beams, as do the  $e^+e^-$  colliders, the phase-space damping due to synchrotron radiation is now absent. Furthermore, since antiprotons are

Table 1. List of parameters (from Ref. [9])

1. MAIN RING (Fermilab)	
- Beam momentum	250 (400) GeV/c
- Equivalent laboratory energy for ( $p\bar{p}$ )	133 (341) TeV
- Accelerating and bunching frequency	53.14 MHz
- Harmonic number	1113
- RF peak voltage/turn	$3.3 \times 10^6$ v
- Residual gas pressure	$< 0.5 \times 10^{-7}$ Torr
- Beta functions at interaction point	3.5 m
- Momentum compaction at int. point	-0 m
- Invariant emittances ( $N_p = 10^{12}$ )	
- longitudinal	3 eV.s
- transverse	$50 \pi \cdot 10^6$ rad.m
- Bunch length	2.3 m
- Design luminosity	$5 \times 10^{29}$ ( $8 \times 10^{29}$ ) $\text{cm}^{-2}\text{s}^{-1}$
2. ANTIPROTON SOURCE (Stochastic Cooling [11])	
- Nominal stored $\bar{p}$ momentum	3.5 GeV/c
- Circumference of ring	100 m
- Momentum acceptance	0.02
- Betatron acceptances	$100 \pi \cdot 10^6$ rad.m
- Bandwidth of momentum stochastic cooling	400 MHz
- Maximum stochastic accelerating RF voltage	3000 v
- Bandwidth of betatron stochastic cooling	200 MHz
Final invariant emittances ( $N_p = 3 \times 10^{10}$ )	
- longitudinal	0.5 eV.s
- transverse	$10 \pi \cdot 10^6$ rad.m

scarce, one has to operate the collider in conditions of relatively large beam-beam interactions, which is not the case for the continuous proton beams of the previously operated Intersecting Storage Rings (ISR) at CERN [12]. One of the most remarkable results of the  $p\bar{p}$  Collider has probably been the fact that it has operated at such high luminosity, which in turn means a large beam-beam tune shift. In the early days of construction, very serious concern had been voiced regarding the instability of the beams due to beam-beam interaction. The beam-beam force can be approximated as a periodic succession of extremely non-linear potential kicks. It is expected to excite a continuum of resonances of the storage ring which has, in principle, the density of rational numbers. Reduced to bare essentials, we can consider the case of a weak antiproton beam colliding head on with a strongly bunched proton beam. The increment, due to the angular kick  $\Delta x'$ , of the action invariant  $W = \gamma x^2 + 2\alpha x x' + \beta x'^2$  of an antiproton is  $\Delta W = \beta(\Delta x') + 2(\alpha x + \beta x')\Delta x'$ , and this can be expressed in terms of the 'tune shift',  $AQ$  as  $\Delta x' = 4\pi\Delta Qx/\beta$ . If we now assume that the successive kicks are randomized, the second term of  $\Delta W$  averages to zero, and we get

$$\langle \Delta W/W \rangle = 1/2(4\pi\Delta Q)^2.$$

For the design luminosity we need  $AQ = 0.003$ , leading to  $(\Delta W/W) = 7.1 \times 10^4$ . This is a very large number indeed, giving an e-fold in-

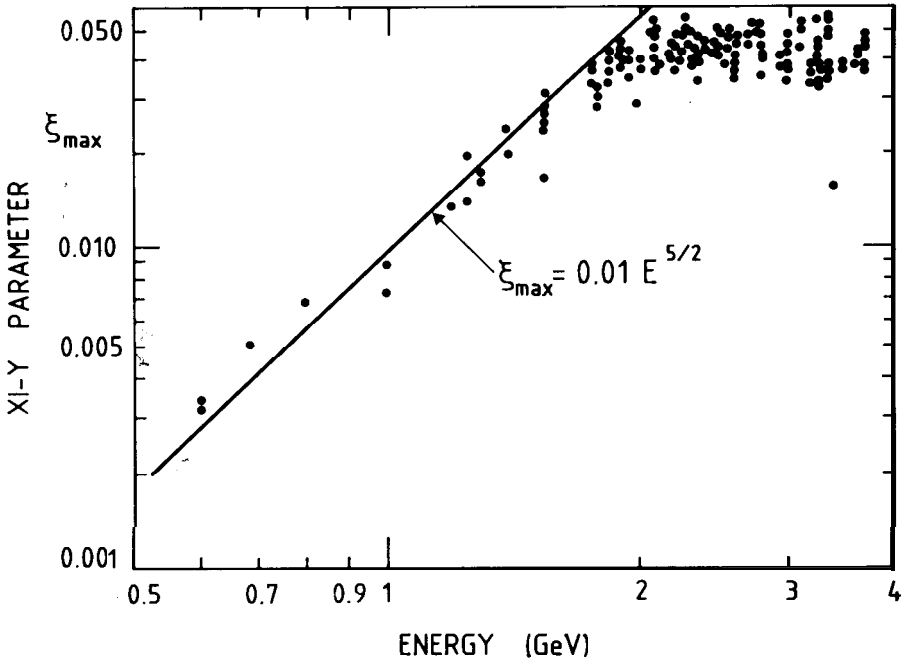


Fig. 6. Maximum allowed beam-beam tune-shift parameter, XI-Y, as a function of energy of the electron-positron collider SPEAR. One can see a dramatic drop in the allowed tune shift at lower energies, as a consequence of the reduced synchrotron damping. Extrapolation to the case of proton-antiproton collisions where the damping is absent and therefore the damping time is constant, is to be identified with the beam lifetime, permitting an infinitesimal tune shift and therefore to an unpractical luminosity.

crease of  $W$  in only  $1/7.1 \times 10^{-4} = 1.41 \times 10^3$  kicks! Therefore the only reason why the antiproton motion remains stable is because these strong kicks are not random but periodic, and the beam has a long 'memory' which allows them to be added coherently rather than at random. Off-resonance, the effects of these kicks then cancel on the average, giving an overall zero amplitude growth. The beam-beam effects are very difficult, if not impossible, to evaluate theoretically, since this *a priori* purely deterministic problem can exhibit stochastic behaviour and irreversible diffusion-like characteristics.

A measurement at the electron-positron collider SPEAR at Stanford had further aggravated the general concern about the viability of the  $p\bar{p}$  collider scheme. Reducing the energy of the electron collider (Fig. 6) resulted in a smaller value of the maximum allowed tune shift, interpreted as being due to the reduced synchrotron radiation damping. Equating the needed beam lifetime for the  $p\bar{p}$  collider (where damping is absent) with the extrapolated damping time of an  $e^+e^-$  collider gives a maximum allowed tune shift  $\Delta Q = 10^{-5} \div 10^{-6}$ , which is catastrophically low. This bleak prediction was not confirmed by the experience at the collider, where  $\Delta Q = 0.003$  per crossing, and six crossings are routinely achieved with a beam luminosity lifetime approaching one day. What, then, is the reason for such a striking contradiction between experiments with protons and those with electrons? The differ-

ence is caused by the presence of synchrotron radiation in the latter case. The emission of synchrotron photons is a major source of quick randomization between crossings and leads to a rapid deterioration of the beam emittance. Fortunately, the same phenomenon also provides us with an effective damping mechanism. The  $p\bar{p}$  collider works because both the randomizing and the damping mechanisms are absent. This unusually favourable combination of effects has ensured that  $p\bar{p}$  colliders have become viable devices. They have the potential for substantial improvements in the future. The accumulation of more antiprotons would permit us to obtain a substantially larger luminosity, and a project is under way at CERN which is expected to be able to deliver enough antiprotons to accumulate, *in one single day*, the integrated luminosity on which the results presented in this lecture have been based ( $\sim 100 \text{ nb}^{-1}$ ).

#### 4. The detection method

The process we want to observe is the one represented in Fig. 2b, namely

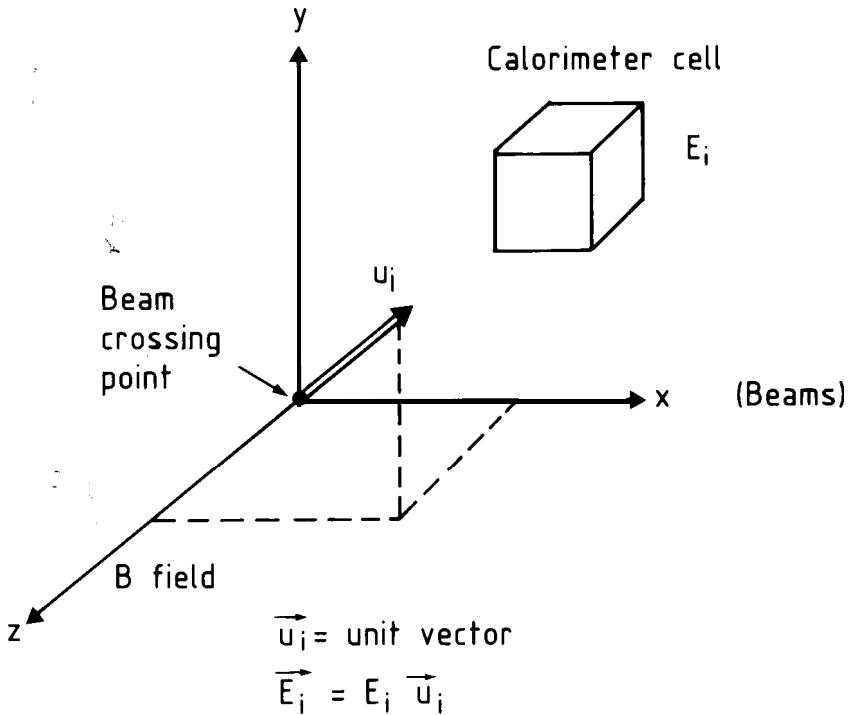
$$p + \bar{p} \rightarrow W^+ + X, \quad W^+ \rightarrow e^+ + \nu_e \quad (3)$$

where X represents the sum of the debris from the interactions of the other protons (spectators). Although the detection of high-energy electrons is relatively straightforward, the observation of neutrino emission is uncommon in colliding-beam experiments. The probability of secondary interactions of the neutrino in any conceivable apparatus is infinitesimal. We must therefore rely on kinematics in order to signal its emission indirectly. This is achieved with an appropriately designed detector [13] which is uniformly sensitive, over the whole solid angle, to all the charged or neutral interacting debris produced by the collision. Since collisions are observed in the centre of mass, a significant momentum imbalance may signal the presence of one or more non-interacting particles, presumably neutrinos.

The method can be conveniently implemented with calorimeters, since their energy response can be made rather uniform for different incident particles. Calorimetry is also ideally suited to the accurate measurement of the energy of the accompanying high-energy electron for process (3). Energy depositions (Fig. 7) in individual cells,  $E_i$ , are converted into an energy flow vector  $\vec{E}_i = \vec{n}_i E_i$ , where  $\vec{n}_i$  is the unit vector pointing from the collision point to (the centre of) the cell. Then, for relativistic particles and for an ideal calorimeter response  $\sum_i \vec{E}_i = 0$ , provided no non-interacting particle is emitted. The sum covers the whole solid angle. In reality there are finite residues to the sum:  $\vec{\Delta E}_M = \sum_i \vec{E}_i$ . This quantity is called the 'missing energy' vector. Obviously in the case of a neutrino emission,  $\vec{p}_\nu^* = -\vec{\Delta E}_M$ . In the case of process (3) the effect is particularly spectacular, since in the centre of mass of the W the neutrino momentum  $p_\nu^* = m_W/2$  is very large.

The practical realization of such a detector [14] is shown in Fig. 8a. After momentum analysis in a large-image drift chamber in a horizontal magnetic field of 7000 G oriented normal to the beam directions, six concentric sets of finely segmented calorimeters (Fig. 8 b) surround the collision point, down to

## CONSTRUCTION OF ENERGY VECTORS



Momentum conservation  $\rightarrow \sum_i \vec{E}_i = 0$   
 (ideal detector)

$$\Delta \vec{E}_m = \sum \vec{E}_i$$

$$\sum |E_T| = \text{event "temperature"}$$

Fig. 7. Principal diagram for constructing energy vectors and the missing energy of the event

angles of  $0.2^\circ$  with respect to the beam directions. The operation of these calorimeters is shown schematically in Fig. 9a. The first four segments are sandwiches of lead and scintillator, in which electrons are rapidly absorbed (Fig. 9b), followed by two sections of iron/scintillator sandwich (which is also the return yoke of the magnetic field). All hadrons are completely absorbed within these calorimeters. Muons are detected by eight planes of large drift chambers which enclose the whole detector volume. If one or more muons are detected, their momenta, measured by magnetic curvature, must be added 'by hand' to the energy flow vector.

The performance of the energy flow measurement has been tested with

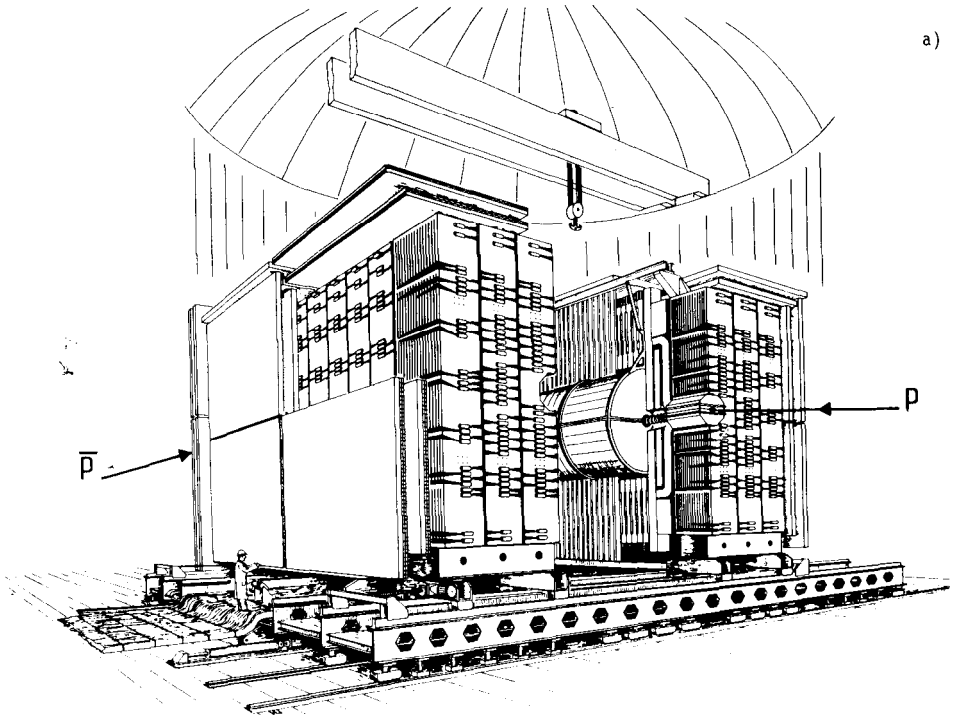


Fig. 8a. The UA1 detector solid-angle is fully covered down to  $0.2^\circ$ .

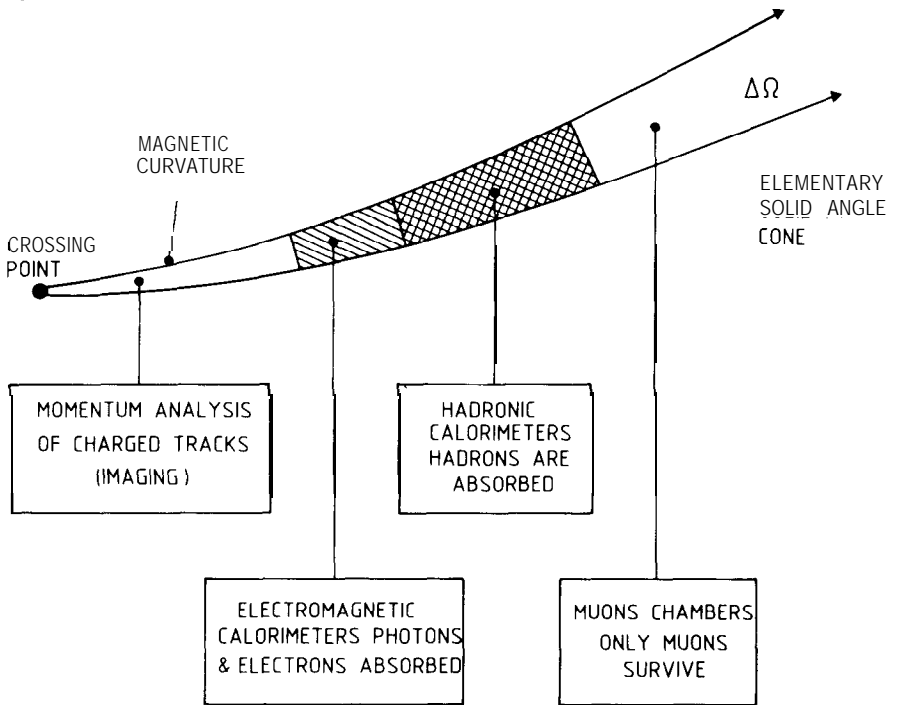


Fig. 8b. The schematic functions of each of the elementary solid-angle elements constituting the detector structure.

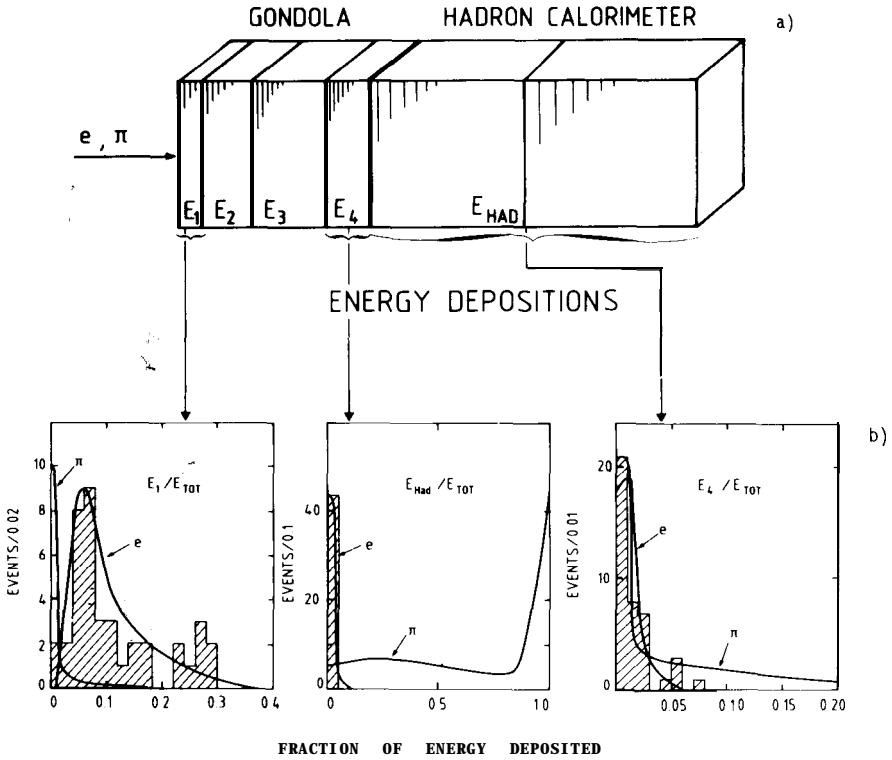


Fig. 9. a) Schema of an elementary solid-angle cell. After four segments of lead/scintillator sandwich, there are two elements of iron/scintillator sandwich, which is also the magnetic field return loop. b) Energy depositions for high-energy pions and electrons. The nature of the particle can be discriminated looking at the transition curve.

standard collisions (minimum bias). Fig. 10 shows how well the vertical component of the missing-energy vector is observed for minimum bias events. The missing energy  $\Delta \vec{E}_M$  resolution for each transverse component can be parametrized as  $\sigma = 0.43 \sqrt{\sum_i E_T^{(i)}}$ , where  $\sum_i E_T^{(i)}$ , in units of GeV, is the scalar sum of the transverse components of the energy flow  $E_T^{(i)}$ . The same parametrization also holds for events which contain high transverse momentum jets, and for which the detector non-uniformities are more critical since energy deposition is highly localized (Fig. 11). The resolution function is shown in Fig. 12, where the missing energy for two-jet events is shown along with a Monte Carlo calculation of the expected distribution based on the expected behaviour of the calorimeters as determined by test-beam data and the measured fragmentation functions of jets.

For a typical event with  $\sum_i E_T^{(i)} = 80$  GeV, we measure the transverse components of  $\Delta \vec{E}_M$  to about 4 GeV. The longitudinal component of the momentum balance will not be used in the present analysis since, in spite of the smallness of the window through which the beam pipes pass ( $\leq 0.2^\circ$ ), energetic particles quite often escape through the aperture.

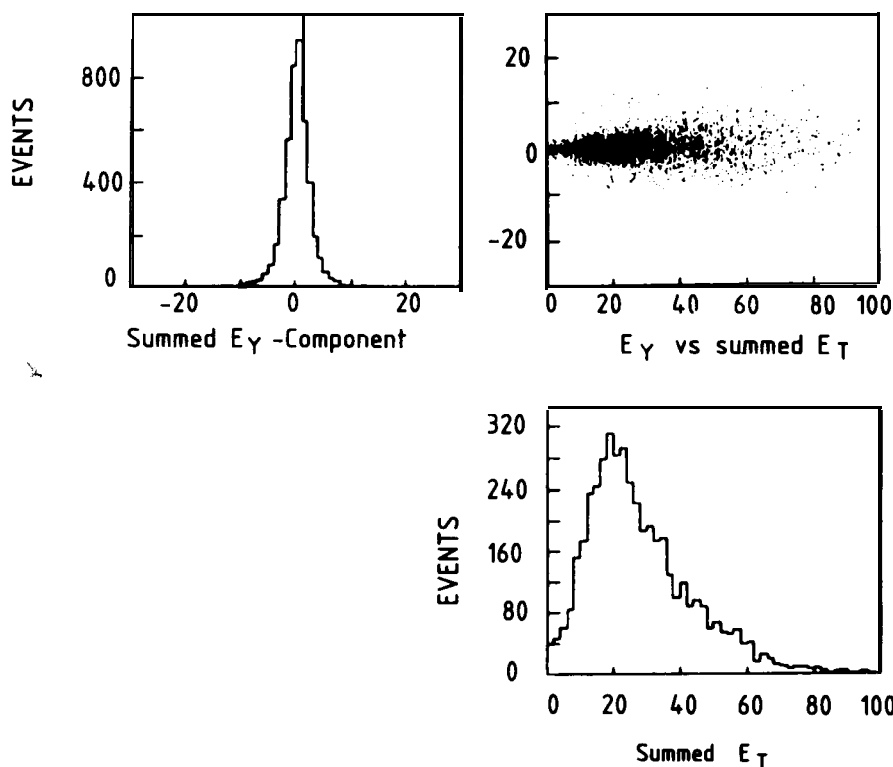


Fig. 10. Scatter-plot of the vertical component of missing transverse energy versus the total transverse energy observed in all calorimeter cells.

### 5. Observation of the $W \rightarrow e + \nu$ signal

The observation by the UA1 Collaboration [15] of the charged intermediate vector boson was reported in a paper published in February 1983, followed shortly by a parallel paper from the UA2 Collaboration [16]. Mass values were given:  $m_w = (80 \pm 5) \text{ GeV}/c^2$  (UA1) and  $m_w = (80_{-6}^{+10}) \text{ GeV}/c^2$  (UA2). Since then, the experimental samples have been considerably increased, and one can now proceed much further in understanding the phenomenon. In particular, the assignment of the events to reaction (3) can now be proved rather than postulated. We shall follow here the analysis of the UA1 events [17].

Our results are based on an integrated luminosity of  $0.136 \text{ pb}^{-1}$ . We first performed an inclusive search for high-energy isolated electrons. The trigger selection required the presence of an energy deposition cluster in the electromagnetic calorimeters at angles larger than  $5^\circ$ , with transverse energy in excess of 10 GeV. In the event reconstruction this threshold was increased to 15 GeV, leading to about  $1.5 \times 10^6$  beam-beam collision events.

By requiring the presence of an associated, isolated track with  $p_T > 7 \text{ GeV}/c$  in the central detector, we reduced the sample by a factor of about 100. Next, a maximum energy deposition (leakage) of 600 MeV was allowed in the hadron calorimeter cells after the electromagnetic counters, leading to a sample of 346

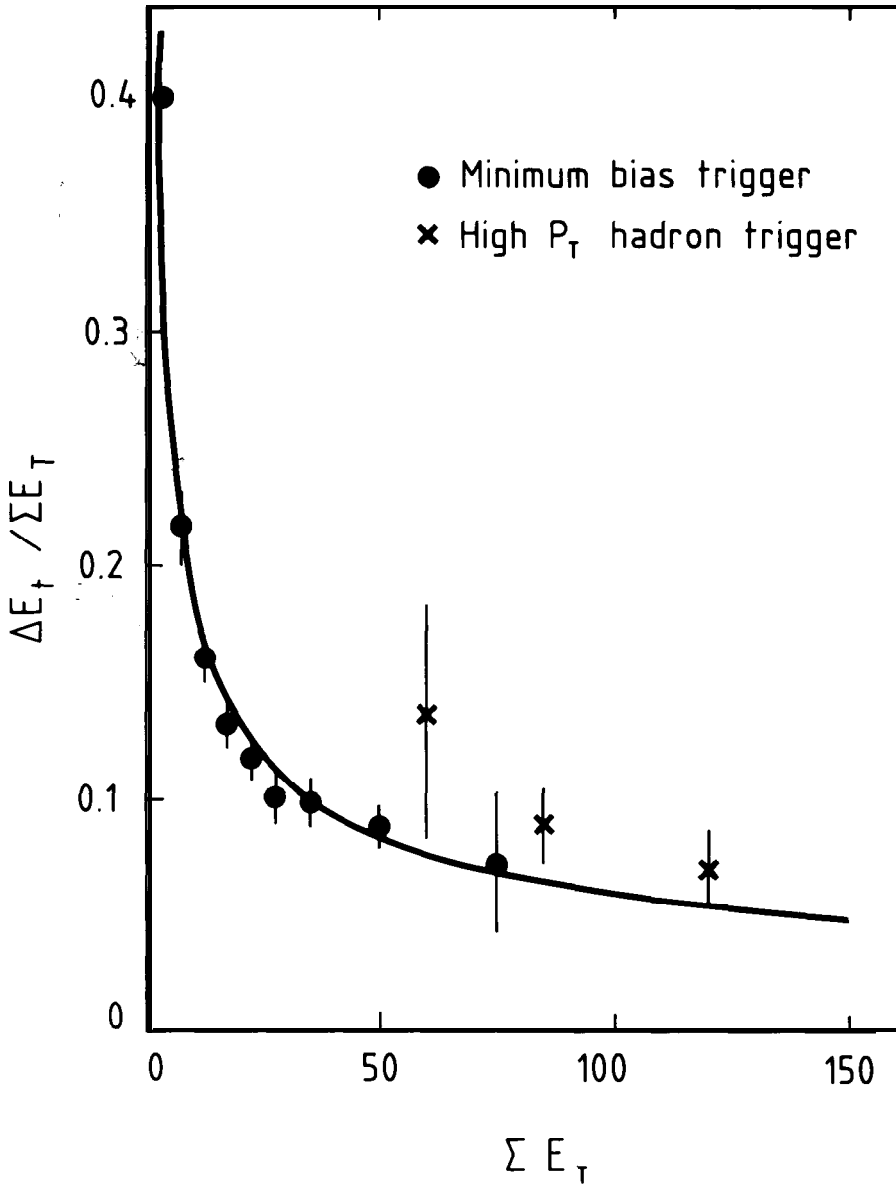


Fig. 11. Missing-energy resolution for minimum-bias and jet events

events. We then classified events according to whether there was prominent jet activity.

We found that in 291 events there was a clearly visible jet within an azimuthal angle cone  $|\Delta\phi| < 30^\circ$  opposite to the 'electron' track. These events were strongly contaminated by jet-jet events in which one jet faked the electron signature and had to be rejected. We were left with 55 events without any jet, or with a jet not back-to-back with the 'electron' within  $30^\circ$ . These events had a very clean electron signature (Fig. 13) and a perfect matching between the point of electron incidence and the centroid in the shower detec-

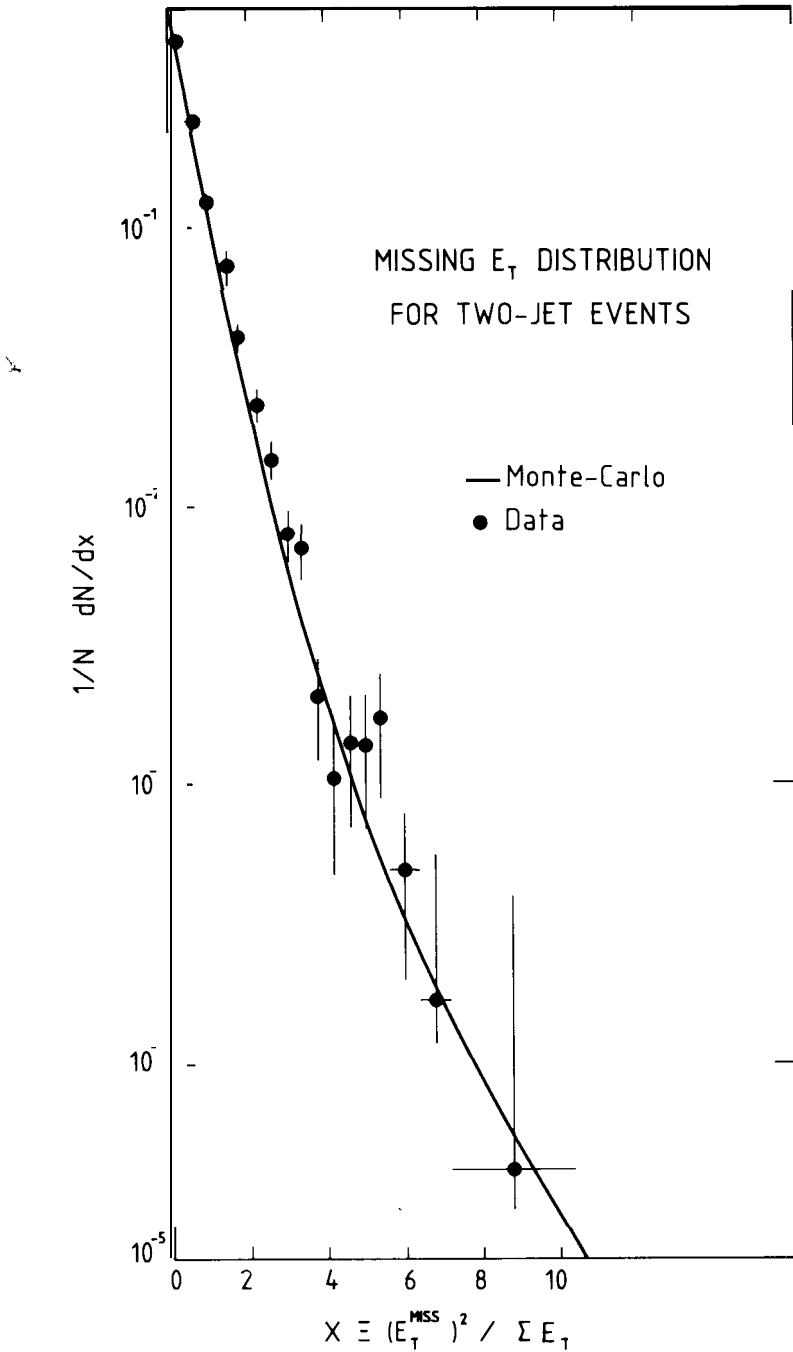


Fig. 12. Transverse energy balance observed for a sample of two-jet events. To convert the horizontal scale to the number of standard deviations ( $n$ ), use the relationship  $n^2 \approx 2x$ . Variables have been chosen in such a way as to transform a Gaussian basic response of the calorimeters into a linear plot. The continuous line is the result of a calculation based on the expected calorimeter responses, as measured with test-beam particles.

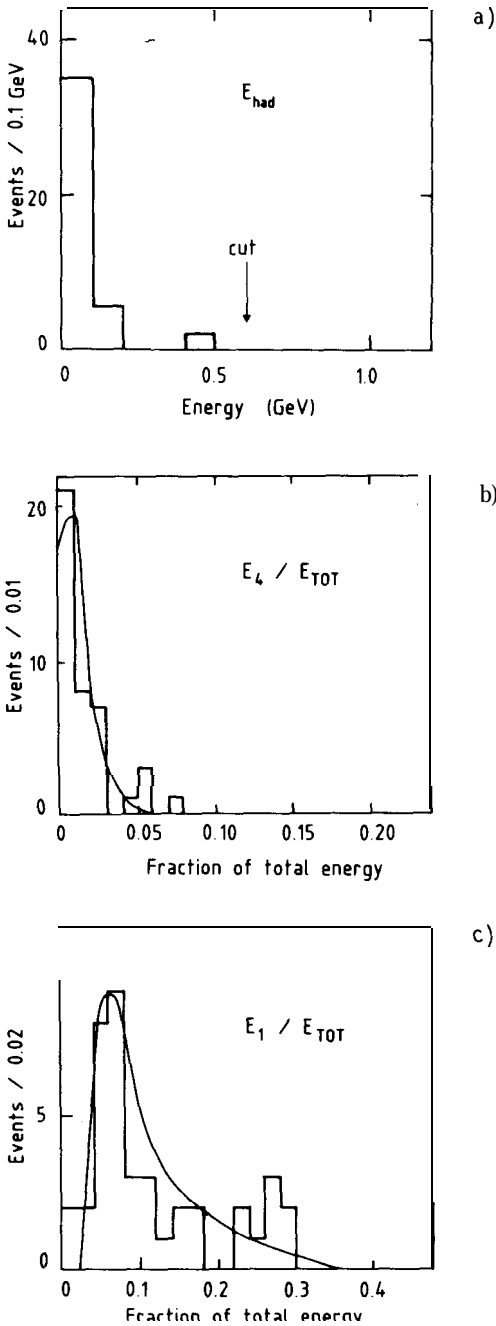


Fig. 13. Distributions showing the quality of the electron signature:

a) The energy deposition in the hadron calorimeter cells behind the 27 radiation lengths (r. l.) of the e.m. shower detector.

b) The fraction of the electron energy deposited in the fourth sampling (6 r.l. deep, after 18 r.l. converter) of the e.m. shower detector. The curve is the expected distribution from test-beam data.

c) As distribution (b) but for the first sampling of the e.m. shower detector (first 6 r.l.).

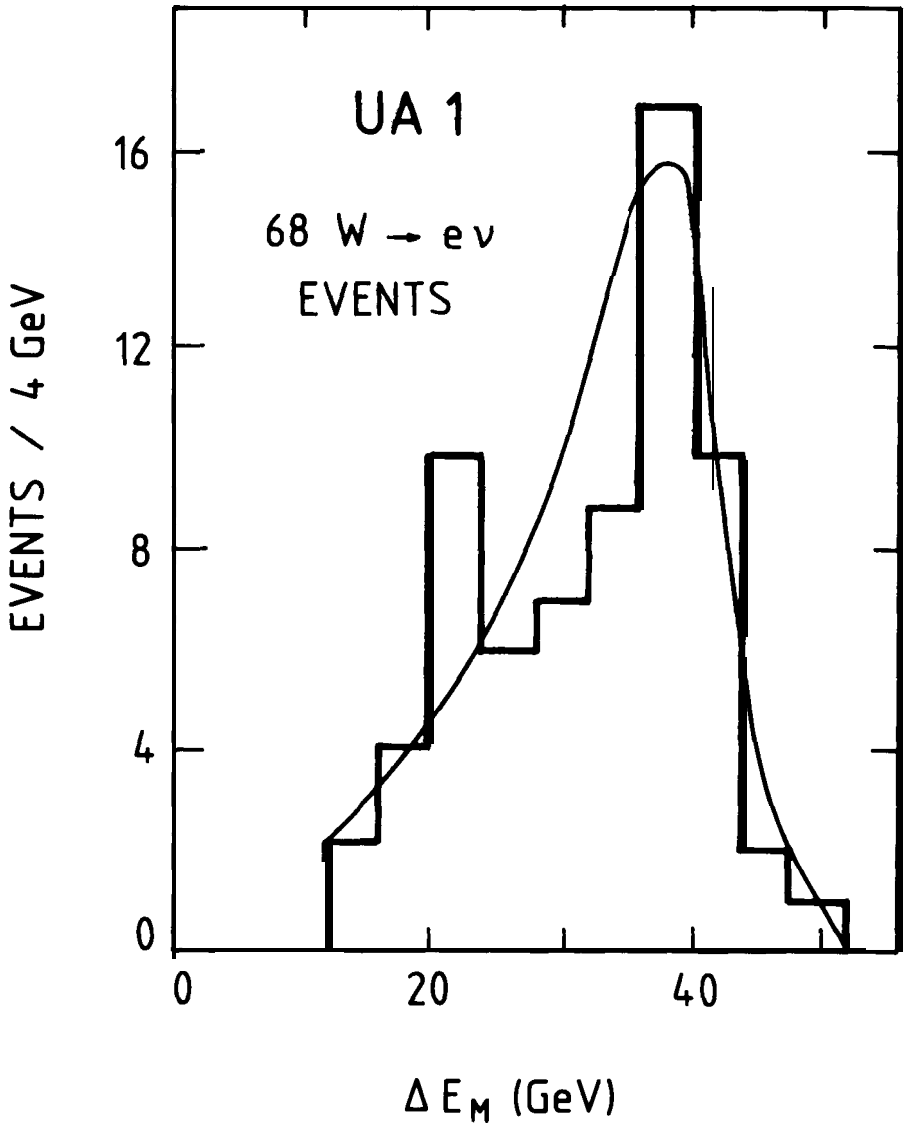


Fig. 14. The distribution of the missing transverse energy for those events in which there is a single electron with  $E_T > 15$  GeV, and no coplanar jet activity. The curve represents the resolution function for no missing energy normalized to the three lowest missing-energy events.

tors, further supporting the absence of composite overlaps of a charged track and neutral  $\pi^0$ 's expected from jets.

The bulk of these events was characterized by the presence of neutrino emission, signalled by a significant missing energy (see Fig. 14). According to the experimental energy resolutions, at most the three lowest missing-energy events were compatible with no neutrino emission. They were excluded by the cut  $E_T^{\text{miss}} > 15$  GeV. We were then left with 52 events.

In order to ensure the best accuracy in the electron energy determination, only those events were retained in which the electron track hit the electromag-

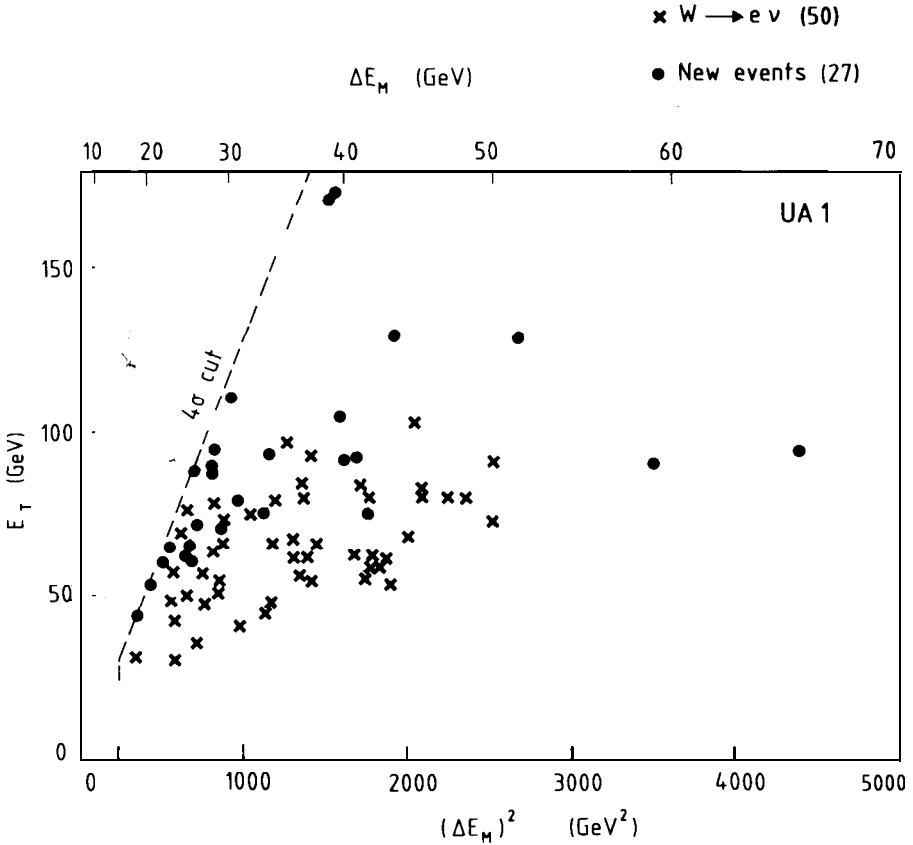


Fig. 15a. Missing transverse energy squared versus  $\Sigma E_T$  for all verified events which have  $\Delta E_m$  more than 4 St. dev. from zero for all events with  $W \rightarrow e+\nu$  decays removed. The events are labelled according to their topology.

netic detectors more than  $\pm 15^\circ$  away from their top and bottom edges. The sample was then reduced to 43 events.

An alternative selection was carried out, based on the inclusive presence of a significant missing energy [18]. This is illustrated in Fig. 15a, where all events with missing energy in excess of 4 standard deviations are shown. One can see that previously selected electron events are found as a subset of the sample. However, a significant number of additional events (twenty-seven) were also recorded, in which there was either a jet or an electromagnetic cluster instead of the isolated electrons (Fig. 15 b). Evidently the inclusive missing-energy definition implies a broader class of physical phenomena (Fig. 16 c) than the simple  $W \rightarrow e+\nu$  decay (Figs. 16a, b). As the study of these events [19] is beyond the scope of this lecture, it will not be pursued any further.

We proceeded to a detailed investigation of the events in order to elucidate their physical origin. The large missing energy observed in all of them was interpreted as being due to the emission of one or several non-interacting neutrinos. A very strong correlation in angle and energy was observed (in the plane normal to the colliding beams, where it could be determined accurately),

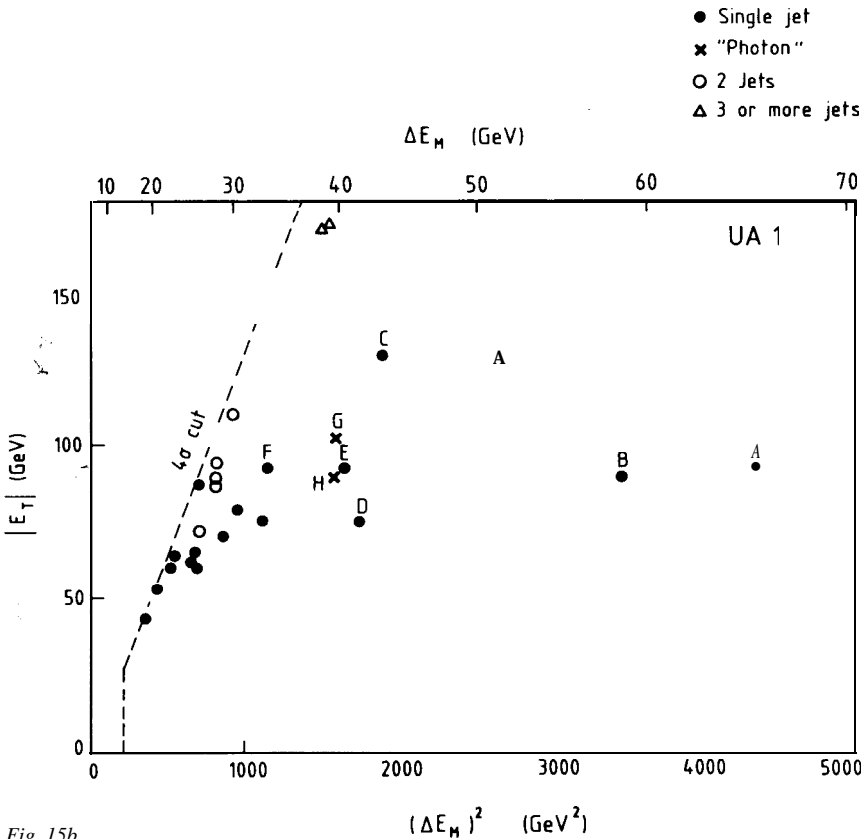


Fig. 15b.

with the corresponding electron quantities, in a characteristic back-to-back configuration expected from the decay of a massive, slow particle (Figs. 17a, b). This suggested a common physical origin for the electron and for one or several neutrinos.

In order to have a better understanding of the transverse motion of the electron-neutrino(s) system, we studied the experimental distribution of the resultant transverse momentum  $p_T^{(W)}$  obtained by adding the neutrino(s) and electron momenta (Fig. 18). The average value was  $p_T^{(W)} = 6.3$  GeV/c. Five events which had a visible jet had also the highest values of  $p_T^{(W)}$ . Transverse momentum balance was almost exactly restored when the vector momentum of the jet was added. The experimental distribution was in good agreement with the many theoretical expectations from quantum chromodynamics (QCD) for the production of a massive state via the Drell-Yan quark-antiquark annihilation [20]. The small fraction (10 %) of events with a jet were then explained as hard gluon bremsstrahlung in the initial state.

Several different hypotheses on the physical origin of the events were tested by looking at kinematical quantities constructed from the transverse variables of the electron and the neutrino(s). We retained two possibilities, namely: i) the two-body decay of a massive particle into the electron and one neutrino,

$$W^- \rightarrow e \bar{\nu}$$

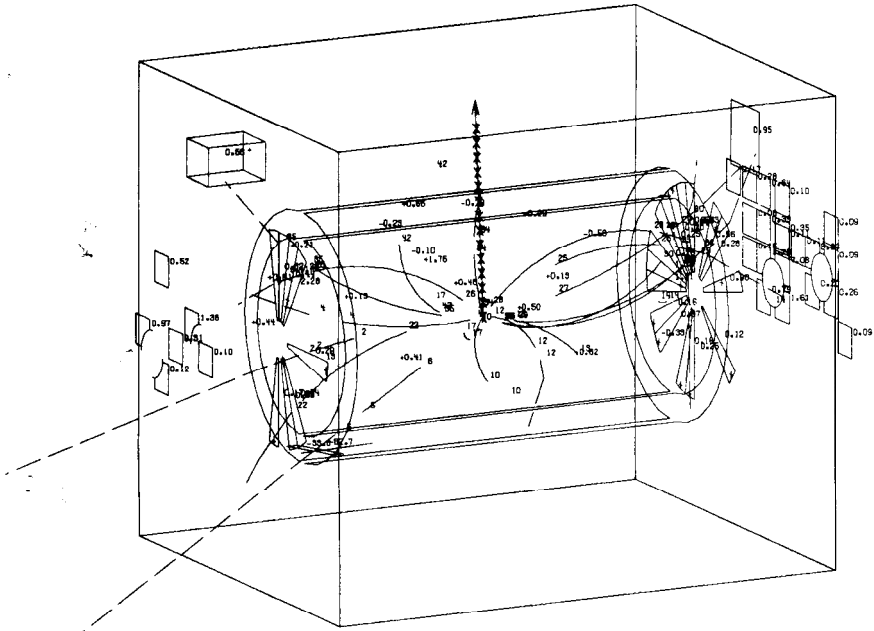


Fig. 16a. Event of the type  $W^- \rightarrow e^- + \bar{\nu}_e$ . All tracks and calorimeter cells are displayed.

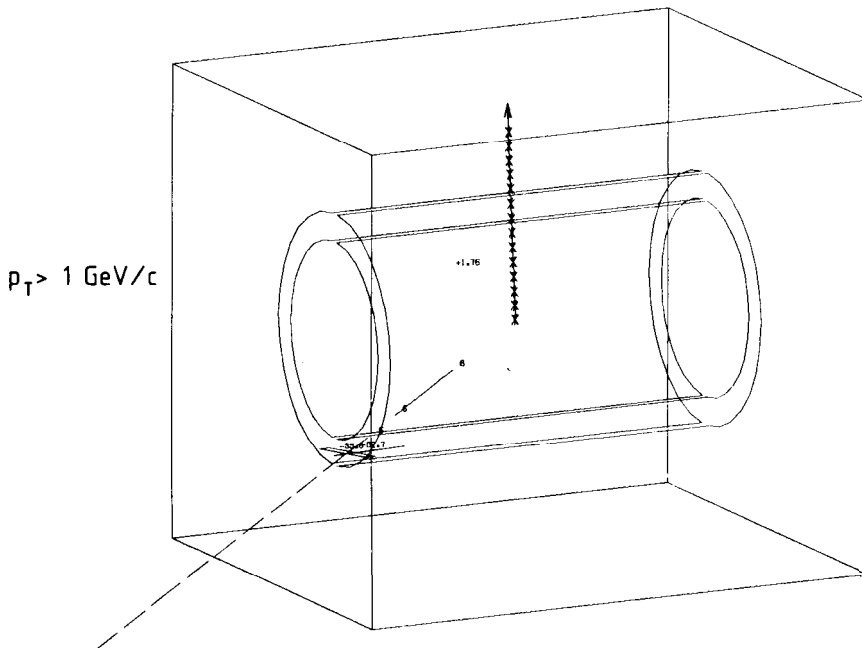


Fig. 16b. The same as picture (a), except that now only particles with  $p_T > 1 \text{ GeV}/c$  and calorimeters with  $E_T > 1 \text{ GeV}$  are shown.

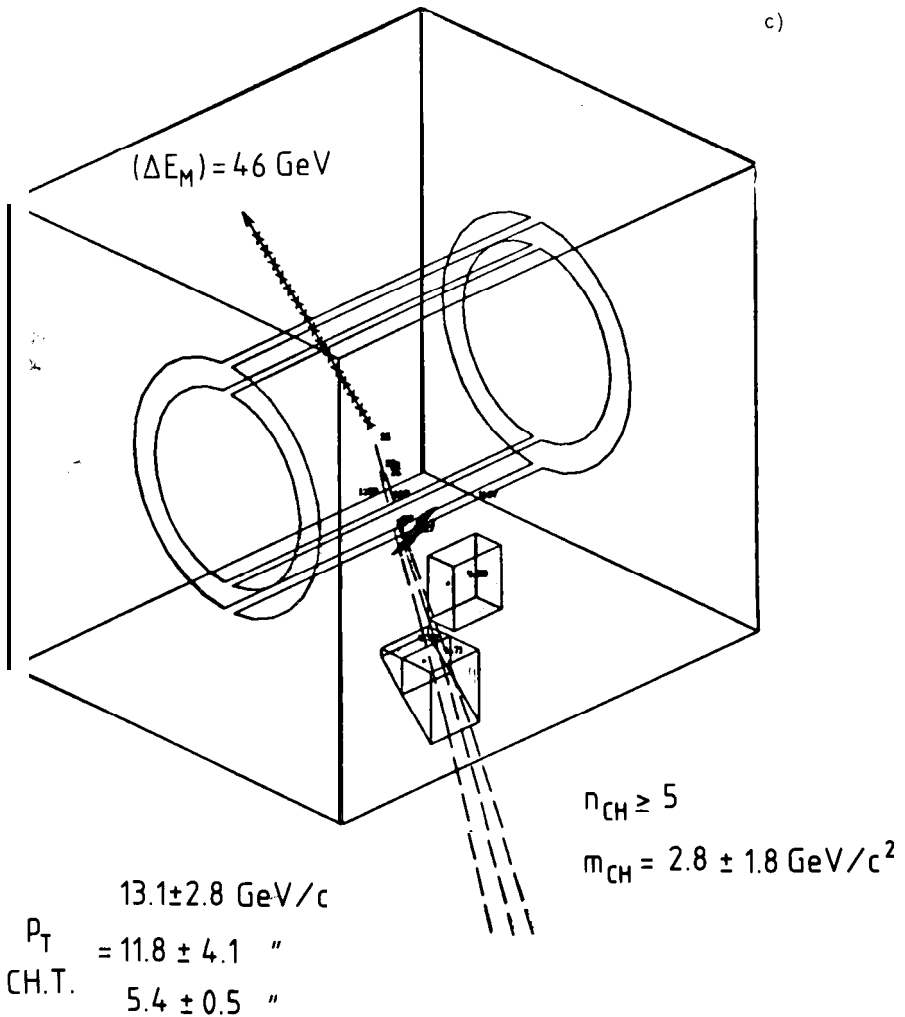


Fig. 16c. Event of the type, jet+missing energy. Only tracks with  $p_T > 1.5 \text{ GeV}/c$  and cells with  $E_c > 1.0 \text{ GeV}$  are displayed.

$W \rightarrow e + \nu_e$ ; and ii) the three-body decay into two, or possibly more, neutrinos and the electron. It can be seen from Figs. 19 a and 19 b that hypothesis (i) is strongly favoured. At this stage, the experiment could not distinguish between one or several closely spaced massive states.

With the help of a sample of isolated hadrons at large transverse momenta, we estimated in detail the possible sources of background coming from ordinary hadronic interactions, and we concluded that they were negligible (0.5 events). (For more details on background, we refer the reader to Ref. 20.) However, we expect to get some background events from other decays of the  $W$ , namely:

$$\begin{aligned} & W \rightarrow \tau + \nu_\tau [\tau \rightarrow \pi^\pm (\pi^0) + \nu_\tau] && (< 0.5 \text{ events}) \\ \text{or} & W \rightarrow \tau + \nu_\tau (\tau \rightarrow e + \nu_e + \nu_\tau) && (= 2 \text{ events}). \end{aligned}$$

a)

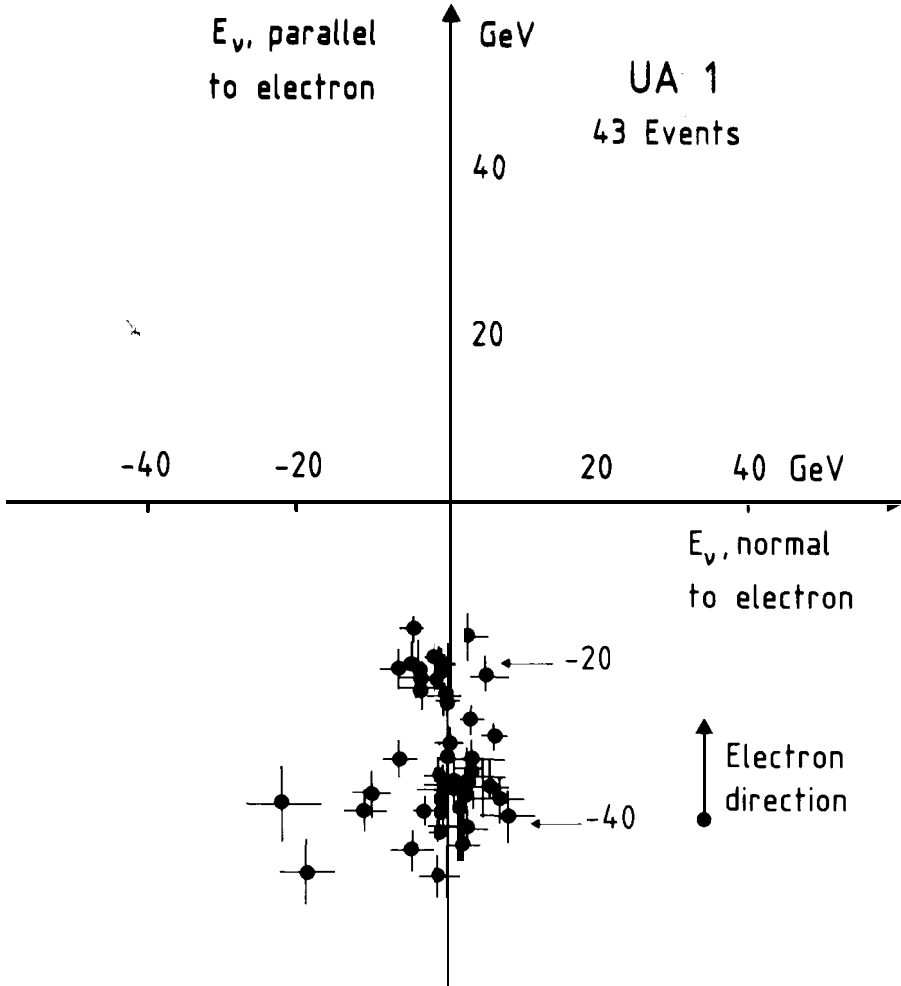


Fig. 17a. Two-dimensional plot of the transverse components of the missing energy (neutrino momentum). Events have been rotated to bring the electron direction to point along the vertical axis. The striking back-to-back configuration of the electron-neutrino system is apparent.

These events were expected to contribute at only the low- $p_T$  part of the electron spectrum, and could even be eliminated in a more restrictive sample.

A value of the  $W$  mass can be extracted from the data in a number of ways:

- i) It can be obtained from the inclusive transverse momentum distribution of the electrons (Fig. 19 a), but the drawback of this technique is that the transverse momentum of the  $W$  particle must be known. Taking the QCD predictions [21], in reasonable agreement with experiment, we obtained  $m_W = (80.5 \pm 0.5) \text{ GeV}/c^2$ .
- ii) We can define a transverse mass variable,  $m_T^2 = 2p_T^{(e)} p_T^{(v)} (1 - \cos \phi)$ , with the property  $m_T \leq m_W$ , where the equality would hold for only those events with no longitudinal momentum components. Fitting Fig. 19b to a

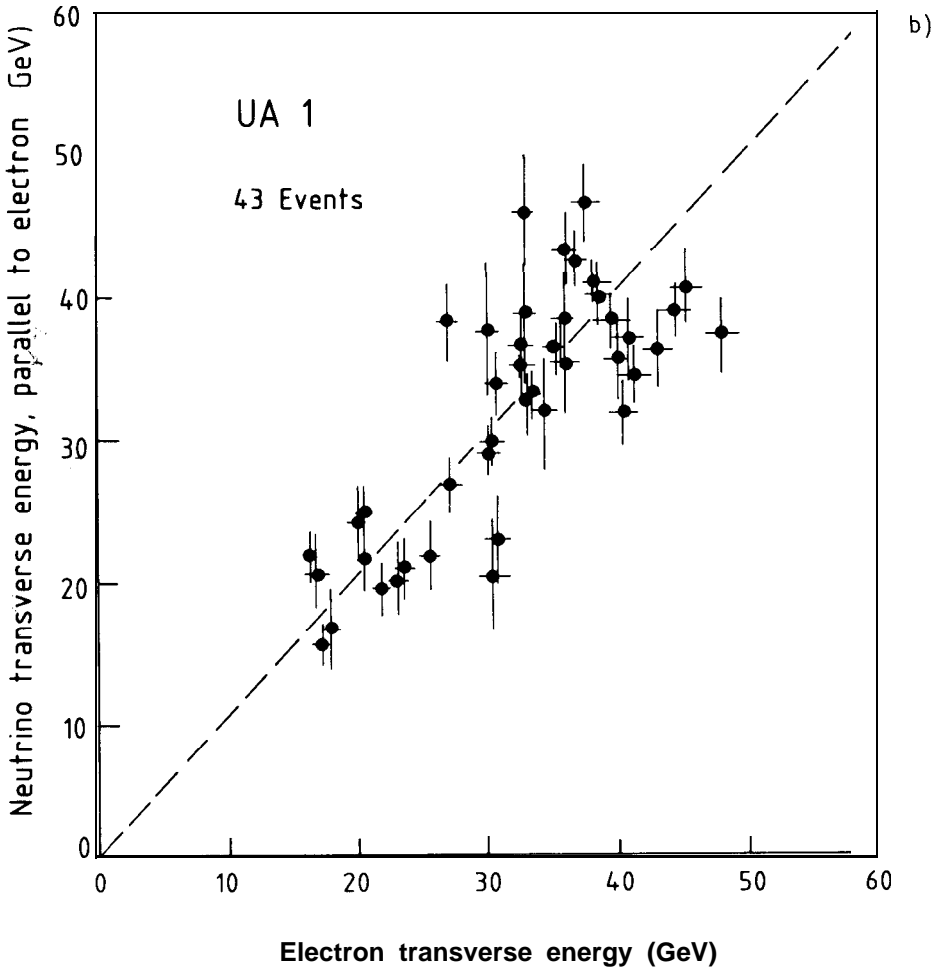


Fig. 17b. Correlation between the electron and neutrino transverse energies. The neutrino component along the electron direction is plotted against the electron transverse energy.

common value of the mass was done almost independently of the transverse motion of the W particles,  $m_w = (80.3^{+0.4}_{-1.3}) \text{ GeV}/c^2$ . It should be noted that the lower part of the distribution in  $m_T^{(W)}$  was slightly affected by  $W \rightarrow \tau + \nu_\tau$  decays and other backgrounds.

- iii) We can define an enhanced transverse mass distribution, selecting only events in which the decay kinematics is largely dominated by the transverse variable with the simple cuts  $p_T^{(e)}, p_T^{(\nu)} > 30 \text{ GeV}/c$ . The resultant distribution (Fig. 19c) then showed a relatively narrow peak at approximately  $76 \text{ GeV}/c^2$ . Model-dependent corrections now only contributed to the difference between this average mass value and the fitted  $m_w$  value,  $m_w = (80.9 \pm 1.5) \text{ GeV}/c^2$ . An interesting upper limit to the width of the W was also derived from the distribution, namely  $\Gamma_T \leq 7 \text{ GeV}/c^2$  (90% confidence level).

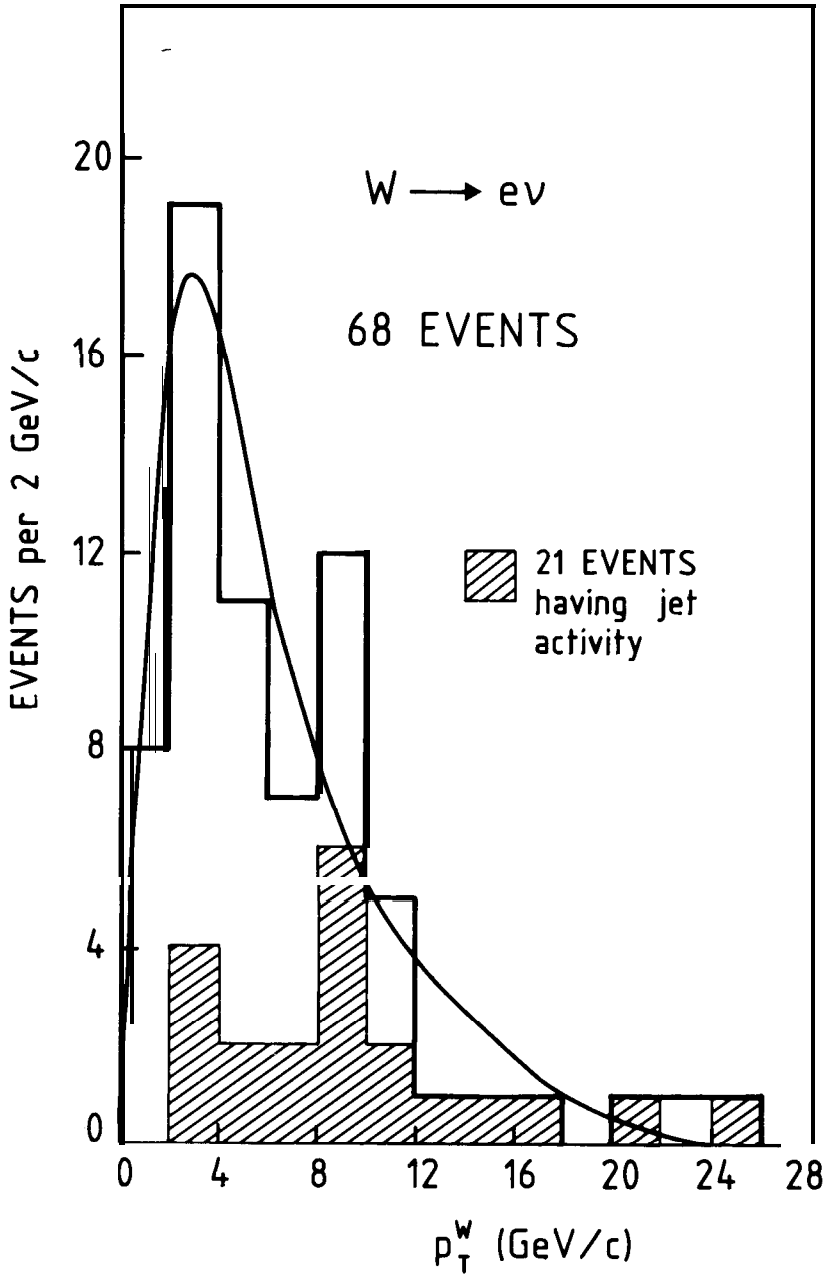


Fig. 18. The transverse momentum distribution of the W derived from our events using the electron and missing transverse energy vectors. The highest  $p_T^{(W)}$  events have a visible jet (shown in black in the figure). The data are compared with the theoretical predictions for W production based on QCD (Ref. [21]).

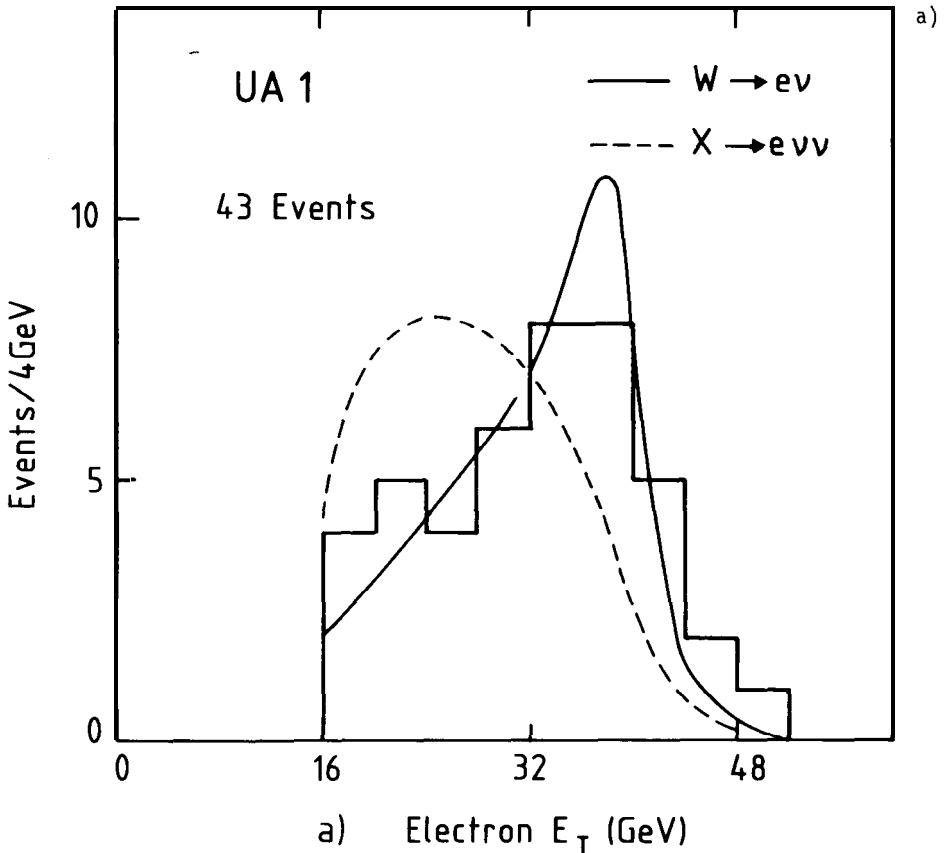


Fig. 19a. The electron transverse energy distribution. The two curves show the results of a fit of the enhanced transverse mass distribution to the hypotheses  $W \rightarrow e + \nu$  and  $X \rightarrow e + \nu + \nu$ . The first hypothesis is clearly preferred.

The three mass determinations gave very similar results. We preferred to retain the result of method (iii), since we believed it to be the least affected by systematic effects, even if it gave the largest statistical error. Two important contributions had to be added to the statistical errors:

- i) *Counter-to-counter calibrations.* They were estimated to be 4% r.m.s. In the determination of the  $W$  mass this effect was greatly attenuated to a negligible level, since many different elements contributed to the event sample.
- ii) *Calibration of the absolute energy scale.* This was estimated to be  $\pm 3\%$ , and of course affects both the  $Z^0$  and the  $W$  samples by the same multiplicative factor.

Once the decay reaction  $W \rightarrow e + \nu_e$  was established, the longitudinal momentum of the electron-neutrino system was determined with a twofold ambiguity for the unmeasured longitudinal component of the neutrino momentum. The overall information of the event was used to establish momentum and energy conservation bounds in order to resolve this ambiguity in 70% of the cases. Most of the remaining events had solutions which were quite close,

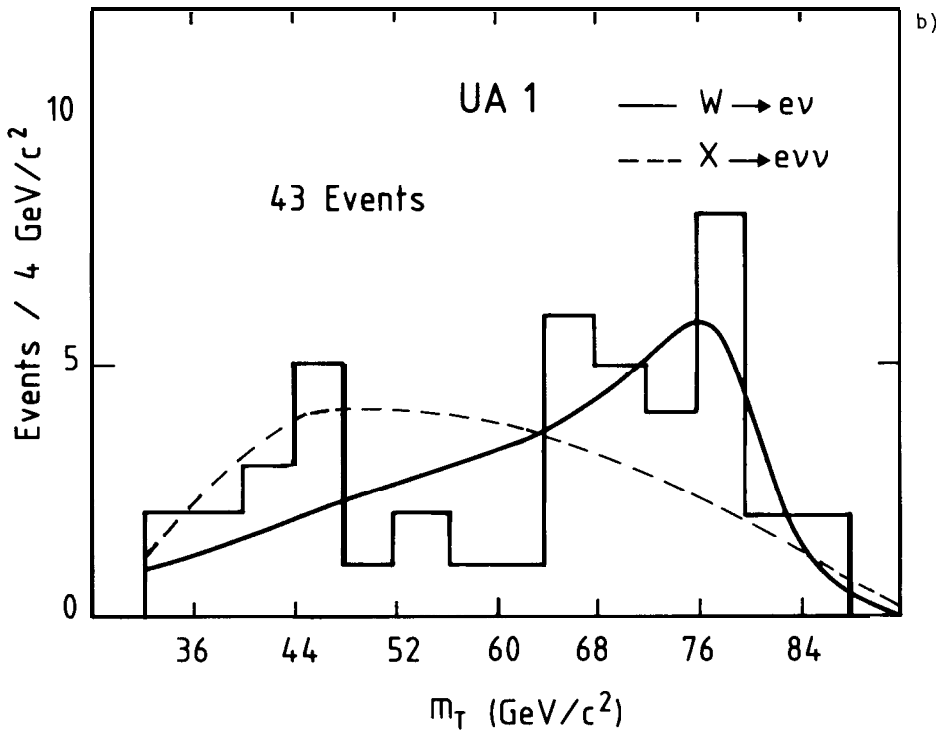


Fig. 19b. The distribution of the transverse mass derived from the measured electron and neutrino vectors. The two curves show the results of a fit to the hypotheses  $W \rightarrow e + \nu$  and  $X \rightarrow e + \nu + \nu$ .

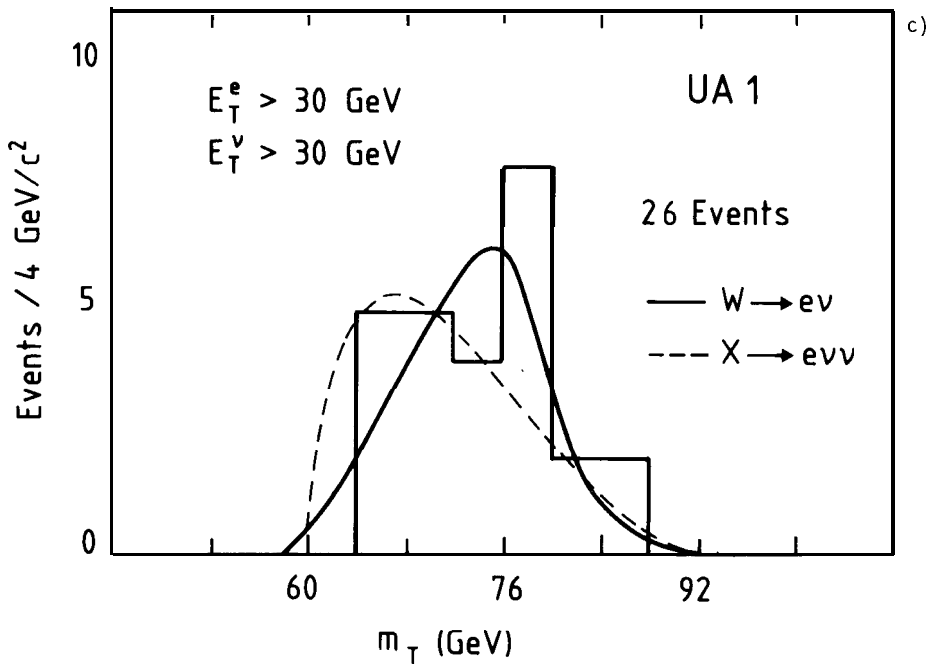
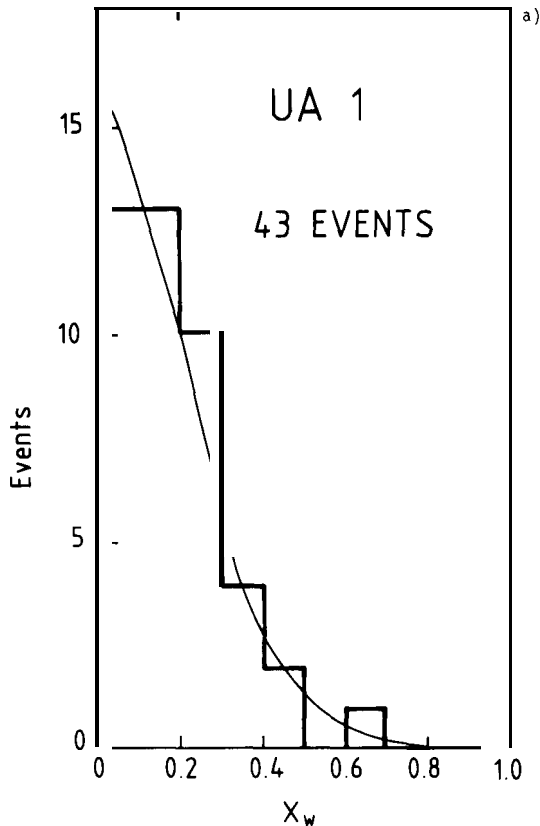


Fig. 19c. The enhanced electron-neutrino transverse mass distribution (see text). The two curves show the results of a fit to the hypotheses  $W \rightarrow e + \nu$  and  $X \rightarrow e + \nu + \nu$ .



**Fig. 20a.** The fractional beam energy  $x_w$  carried by the  $W$ . The curve is the prediction obtained by assuming that the  $W$  has been produced by  $q\bar{q}$  fusion. Note that in general there are two kinematic solutions for  $x_w$  (see text), which are resolved in 70 % of the events by consideration of the energy flow in the rest of the event. Where this ambiguity has been resolved, the preferred kinematic solution has been the one with the lowest  $x_w$ . In the 30 % of the events where the ambiguity is not resolved, the lowest  $x_w$  solution has therefore been chosen.

and the physical conclusions were nearly the same for both solutions. The fractional beam energy  $x_w$  carried by the  $W$  particle is shown in Fig. 20a, and it appears to be in excellent agreement with the hypothesis of  $W$  production in  $q\bar{q}$  annihilation [22]. Using the well-known relations  $x_w = x_p - x_{\bar{p}}$  and  $x_p \cdot x_{\bar{p}} = m_W^2/s$ , we determined the relevant parton distributions in the proton and antiproton. It can be seen that the distributions are in excellent agreement with the expected  $x$  distributions for quarks and antiquarks in the proton and antiproton, respectively (Figs. 20b and 20c). Contributions of the  $u$  and  $d$  quarks were also neatly separated by looking at the charges of produced  $W$  events, since  $(u\bar{d}) \rightarrow W^-$  and  $(\bar{u}d) \rightarrow W^+$  (Figs. 20d and 20e).

#### 6. Observation of the parity (charge conjugation) violation, and determination of the spin of the $W$ particle

One of the most relevant properties of weak interactions is the violation of parity and charge conjugation. Evidently the  $W$  particle, in order to mediate

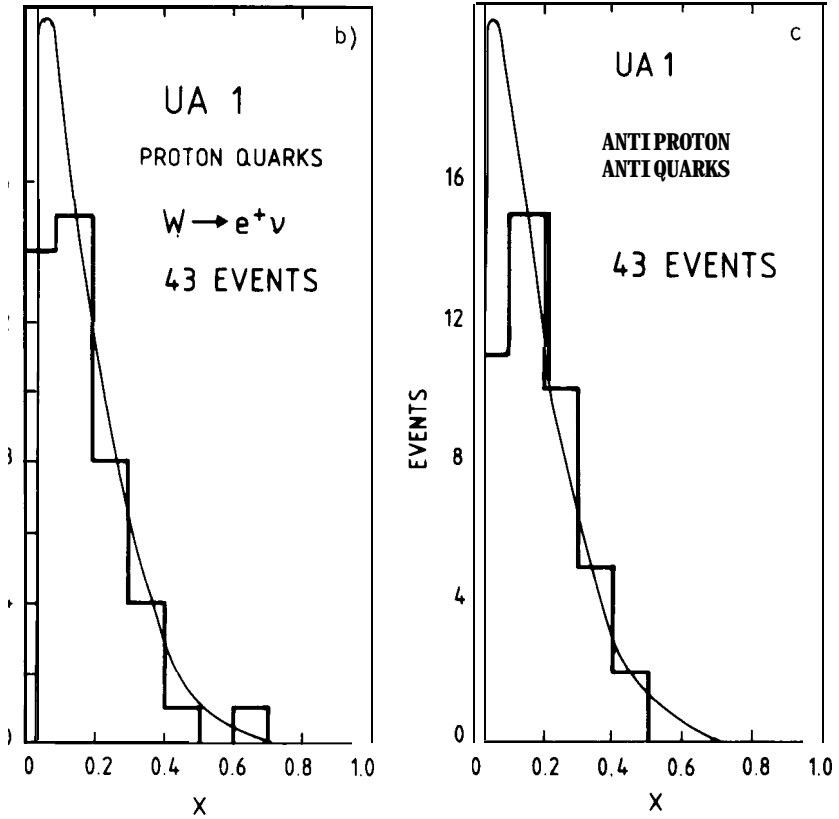


*Fig. 206.* The  $x$ -distribution of the proton quarks producing the  $W$  by  $qq$  fusion. The curve is the prediction assuming  $qq$  fusion.

*Fig. 20c.* The same as *Fig. 20 b* for the antiproton quarks.

weak processes, must also exhibit these properties. Furthermore, as already mentioned, the  $V-A$  nature of the four-fermion interaction implies the assignment  $J=1$  for its spin. Both of these properties must be verified experimentally. According to the  $V-A$  theory, **weak** interactions should act as a longitudinal polarizer of the  $W$  particles, since quarks (antiquarks) are provided by the proton (antiproton) beam. Likewise, decay angular distributions from a polarizer are expected to have a large asymmetry, which acts as a polarization analyser. A strong backward-forward asymmetry is therefore expected, in which electrons (positrons) prefer to be emitted in the direction of the proton (antiproton). In order to study this effect independently of  $W$ -production mechanisms, we have looked at the angular distribution of the emission angle  $\theta^*$  of the electron (positron) with respect to the proton (antiproton) direction in the  $W$  centre of mass. Only events with no reconstruction ambiguity can be used. We verified that this does not bias the distribution in the variable  $\cos \theta^*$ . According to the expectations of  $V-A$  theory the distribution should be of the type  $(1+\cos \theta^*)^2$ , in excellent agreement with the experimental data (*Fig. 21*). The parity violation parameters and the spin of the  $W$  particle can be

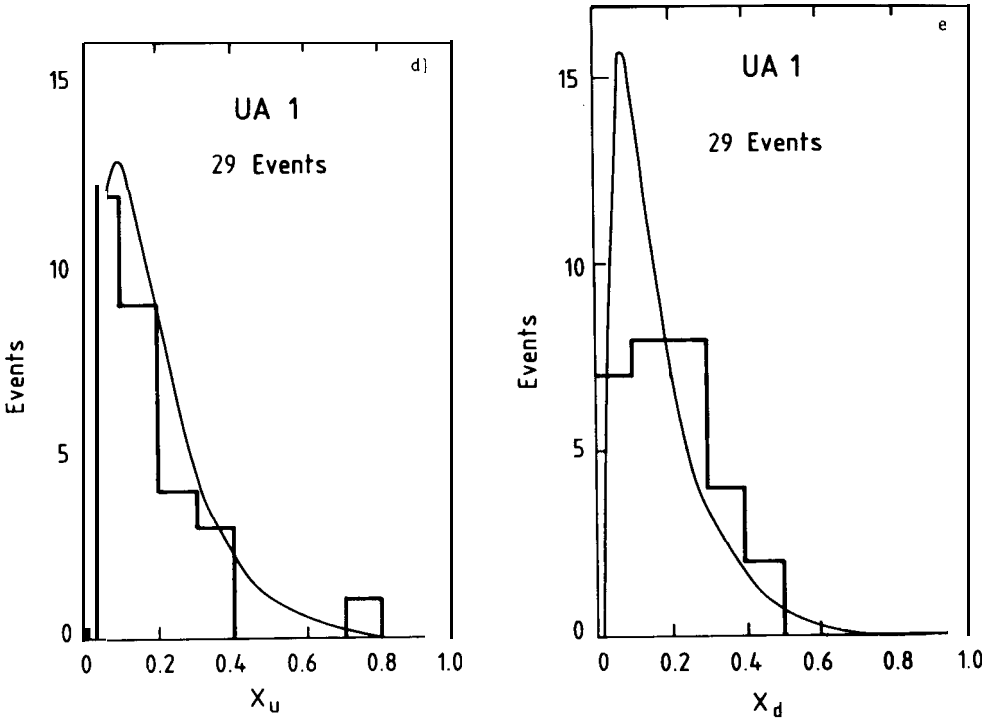


Fig. 20d. The same as Fig. 20 b but for u( $\bar{u}$ ) quarks in the proton (antiproton).  
 Fig. 20e. The same as Fig. 20 b but for d( $\bar{d}$ ) quarks in the proton (antiproton).

determined directly. It has been shown by Jacob [23] that for a particle of arbitrary spin  $J$ , one expects

$$\langle \cos \theta^* \rangle = \langle \lambda \rangle \langle \mu \rangle / J(J+1),$$

where  $\langle \mu \rangle$  and  $\langle \lambda \rangle$  are the global helicity of the production system ( $ud$ ) and of the decay system ( $e\nu$ ), respectively.

For V-A, we then have  $\langle \lambda \rangle = \langle \mu \rangle = -1$ ,  $J = 1$ , leading to the maximal value  $\langle \cos \theta^* \rangle = 0.5$ . For  $J = 0$  it is obvious that  $\langle \cos \theta^* \rangle = 0$ ; and for any other spin value  $J \geq 2$ ,  $\langle \cos \theta^* \rangle \leq 1/6$ . Experimentally we find  $\langle \cos \theta^* \rangle = 0.5 \pm 0.1$ , which supports both the  $J = 1$  assignment and maximal helicity states at production and decay. Note that the choice of sign  $\langle \mu \rangle = \langle h \rangle = \pm 1$  cannot be separated, i.e. right- and left-handed currents, both at production and decay, cannot be resolved without a polarization measurement.

### 7. Total cross-section and limits to higher mass $W$ 's

The integrated luminosity of the experiment was  $136 \text{ nb}^{-1}$ , and it is known to about  $\pm 15 \%$  uncertainty. In order to get a clean  $W \rightarrow e\nu_e$  sample we selected 47 events with  $p_T^{(e)} > 20 \text{ GeV}/c$ . The  $W \rightarrow \tau\nu_\tau$  contamination in the sample was estimated to be  $2 \pm 2$  events. The event acceptance was computed to be 0.65, primarily because of i) the  $p_T^{(e)} > 20 \text{ GeV}/c$  cut (0.80); ii) the jet veto require-

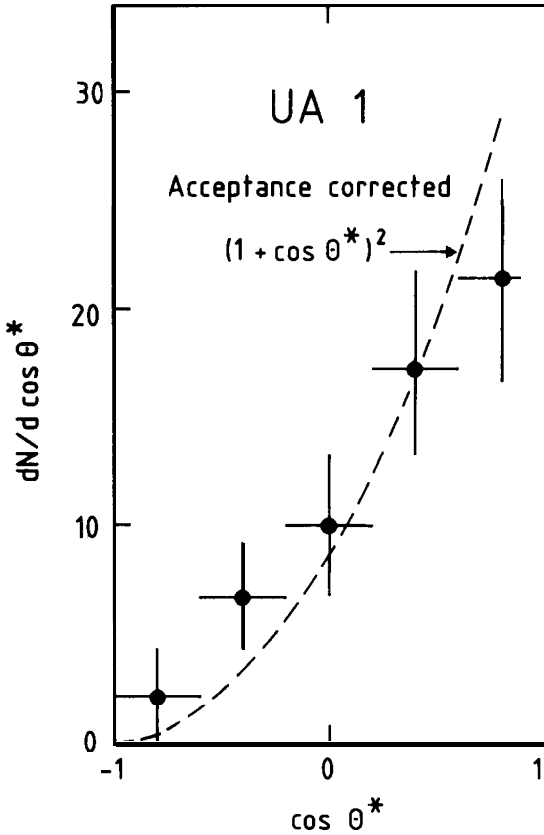


*Fig. 21.* The angular distribution of the electron emission angle  $\theta^*$  in the rest frame of the W after correction for experimental acceptance. Only those events have been used in which the electron charge is determined and the kinematic ambiguity (see text) has been resolved. The latter requirement has been corrected for in the acceptance calculation.

ment within  $\Delta\phi = \pm 30^\circ$  ( $0.96 \pm 0.02$ ); iii) the electron-track isolation requirement ( $0.90 \pm 0.07$ ); and iv) the acceptance of events due to geometry ( $0.94 \pm 0.03$ ). The cross-section was then

$$(\sigma \cdot B)_W = 0.53 \pm 0.08 (\pm 0.09) \text{ nb},$$

where the last error takes into account systematic errors. This value is in excellent agreement with the expectations for the Standard Model [22]:  $(\sigma \cdot B)_W = 0.39 \text{ nb}$ .

No event with  $p_T^{(e)}$  or  $p_T^{(v)}$  in excess of the expected distribution for  $W \rightarrow e\nu$  events was observed. This result can be used to set a limit to the possible existence of very massive W-like objects ( $W'$ ) decaying into electron-neutrino pairs. We found  $(\sigma \cdot B)_{W'} \leq 30 \text{ pb}$  at 90% confidence level, corresponding to  $m_{W'} > 170 \text{ GeV}/c^2$ , when standard couplings and quark distributions were used to evaluate the cross-sections.

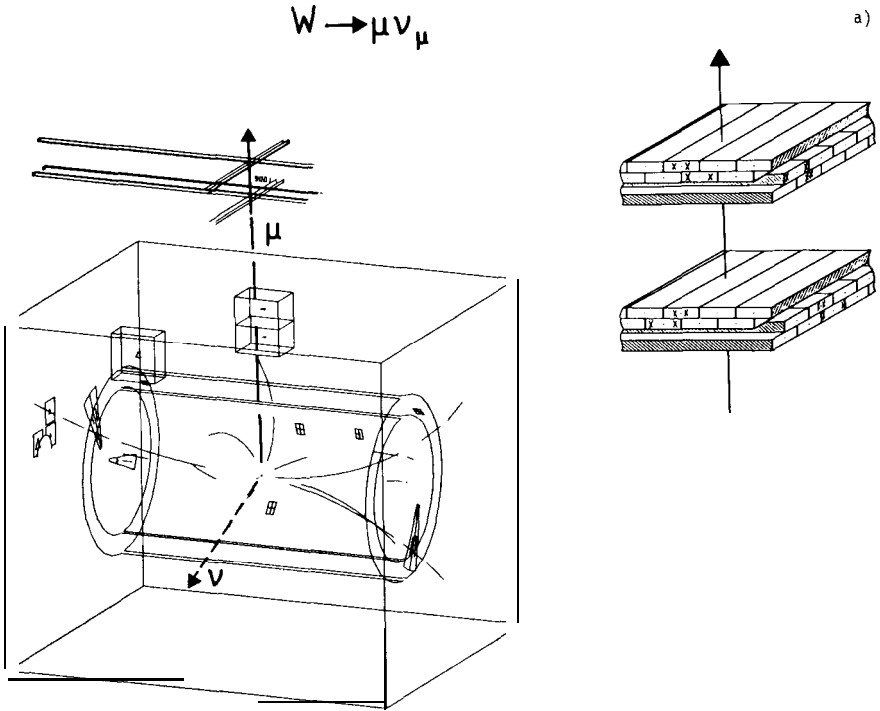


Fig. 22. Examples of decay modes of the W particle:

a)  $W \rightarrow \mu + \nu_\mu$ ; b)  $W \rightarrow \tau + \nu_\tau$ ; c)  $W \rightarrow c + \bar{s}$ ; d)  $W \rightarrow t + b$  ( $t \rightarrow b + e + \nu$ ). For the events of type (d), one can reconstruct the invariant masses of the W particle and of the decaying t-quark jet (Fig. 22 e).

### 8. Universality of the W coupling

The W field should exhibit a universal coupling strength for all the fundamental lepton doublets and all the quark doublets. This implies - apart from small phase-space corrections - equality of the branching ratios of the decay processes

$$W \rightarrow e \nu_e, \tag{4 a}$$

$$W \rightarrow \mu \nu_\mu, \tag{4 b}$$

$$W \rightarrow \tau \nu_\tau. \tag{4c}$$

Likewise, in the case of the quark decay channels

$$W \rightarrow u d_C, \tag{4d}$$

$$W \rightarrow c s_C, \tag{4e}$$

$$W \rightarrow t b_C, \tag{4f}$$

where t is the sixth quark (top quark) provided it exists within the kinematic range of reaction (4f). Neglecting phase-space corrections, which are probably

$$W \rightarrow \tau \nu_\tau$$

$$\quad \quad \quad \downarrow$$

$$\quad \quad \quad \text{Jet} + \bar{\nu}_\tau$$

b)

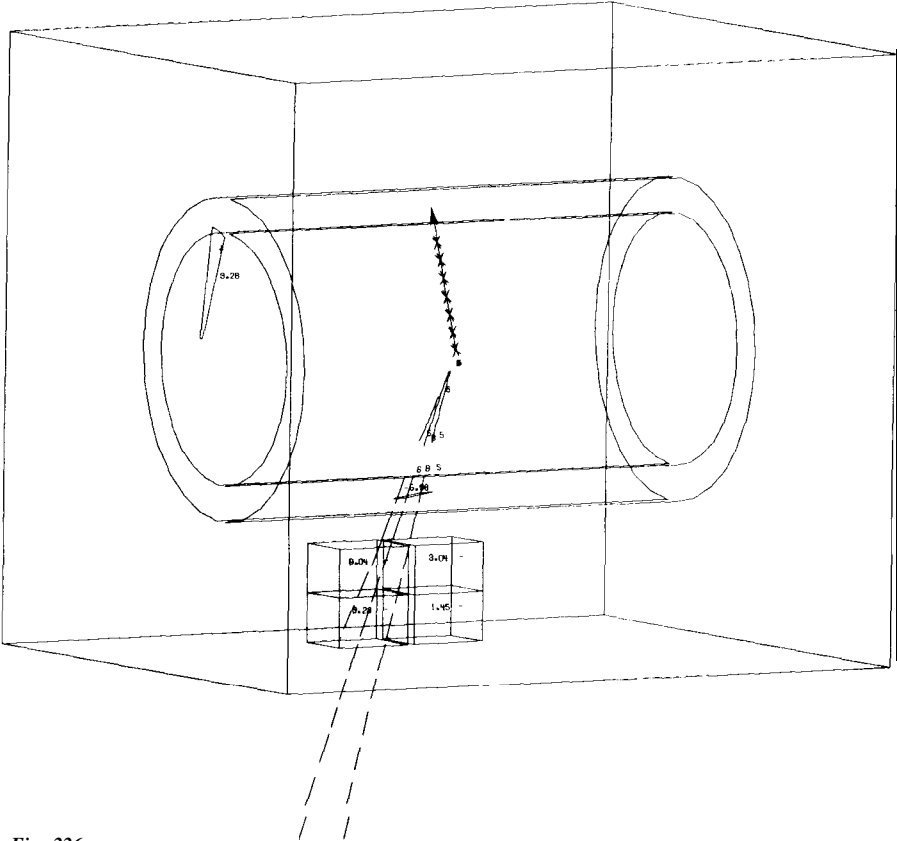


Fig. 226.

important for reaction (4f), we expect equality of the branching ratios, with an overall factor of 3 of enhancement with respect to leptonic channels [(4a) to (4c)] due to colour counting. The subscript C in channels (4d) to (4f) indicates the presence of the Cabibbo mixing. Reactions (4a) and (4d) are implied by the results of Section 5. Reactions (4 b), (4c), and (4e) have been observed, and within about  $\pm 20\%$  they appear to have the correct branching ratios. Some events which are believed to be evidence for the process (4f) have also been reported [24]. They are interpreted for the reaction

$$W \rightarrow t + \bar{b}_C (t \rightarrow b_C + l + \nu) \quad (l \equiv \text{electron or muon}).$$

The  $\bar{b}_C$  and  $b_C$  quarks are 'hadronized' into jets. Data are roughly consistent with  $m_t \approx 40 \text{ GeV}/c^2$ . Examples of reactions (4 b), (4 c), (4 e), and (4f) are shown in Figs. 22a-d, respectively.

Therefore, within the limited statistics there is evidence for universality.

$$W \longrightarrow c\bar{s}$$

c)

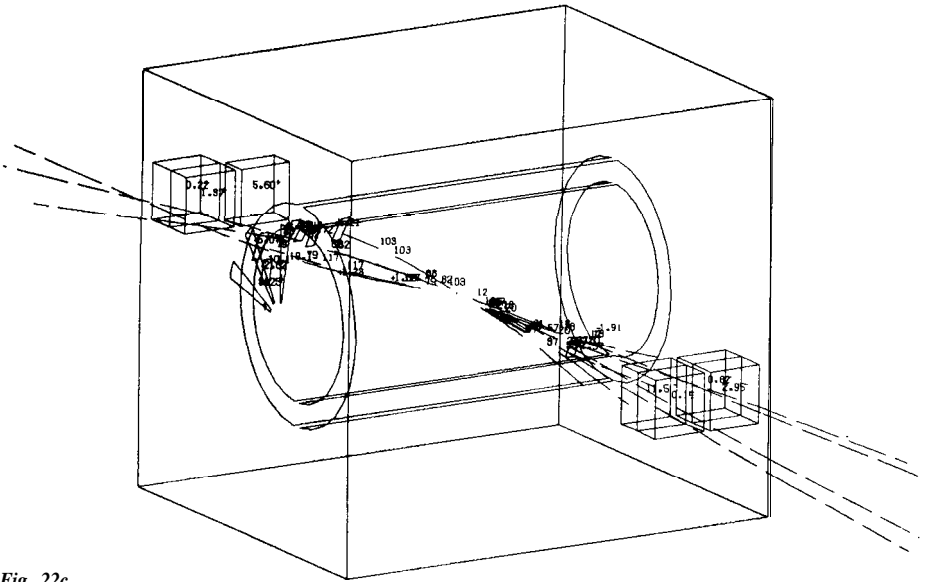


Fig. 22c.

9. Can we derive weak interactions from W-particle observations?

A number of properties of weak interactions as determined by low-energy experiments can now be explained as a consequence of the experimentally observed properties of the W particles. Indeed we know that  $W^-$  must couple to valence quarks at production and to  $(e, \nu_e)$  pairs at decay, which implies the existence of the beta-decay processes  $n \rightarrow p + e^- + \nu_e$  and  $(p) \rightarrow (n) + e^+ + \nu_e$ . The mass value  $m_w$  and the cross-section measurement can then be used to calculate  $G_F$ , the Fermi coupling constant:  $G_F = (1.2 \pm 0.1) \times 10^{-5} \text{ GeV}^{-2}$ . Thus the W-pole saturates the observed weak interaction rate. The interaction must be vector since  $J = 1$ , and parity is maximally violated since  $\langle \mu \rangle = \langle \lambda \rangle = \pm 1$ . The only missing element is the separation between V+A and V-A alternatives. For this purpose a polarization measurement is needed. It may be accomplished in the near future by studying, for instance, the decay  $W \rightarrow \tau + \nu_\tau$  and using the  $\tau$  decay as the polarization analyzer or producing intermediate vector bosons (IVBs) with longitudinally polarized protons.

The universality of couplings and the decay modes of particles of different flavours into different lepton families can also be expected on the basis of the observations of the other decay modes of the W particles.

10. Observation of the neutral boson  $Z^0$

We extended our search to the neutral partner  $Z^0$ , responsible for neutral currents. As in our previous work, production of IVBs was achieved with proton-antiproton collisions at  $\sqrt{s} = 540 \text{ GeV}$  in the UAl detector, except

EVENT 7443/509

d)

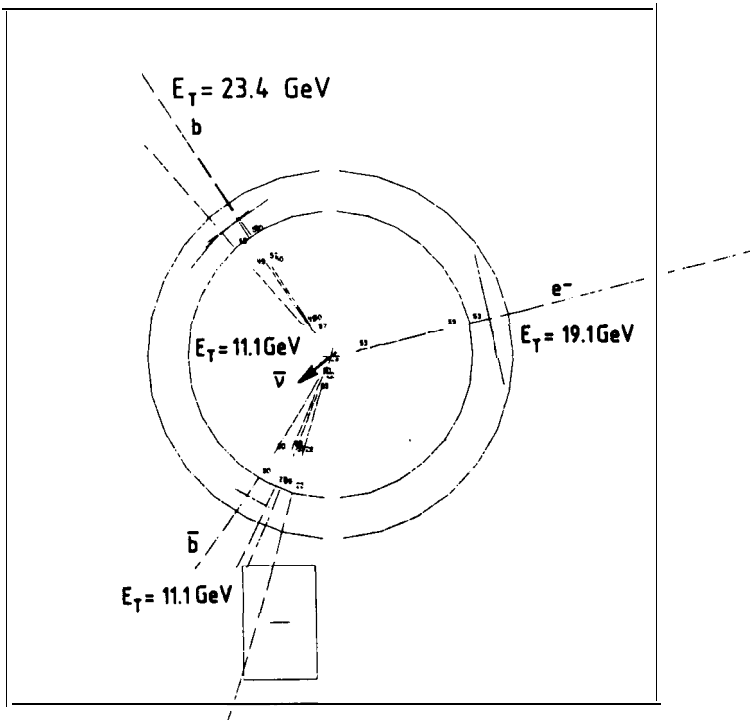
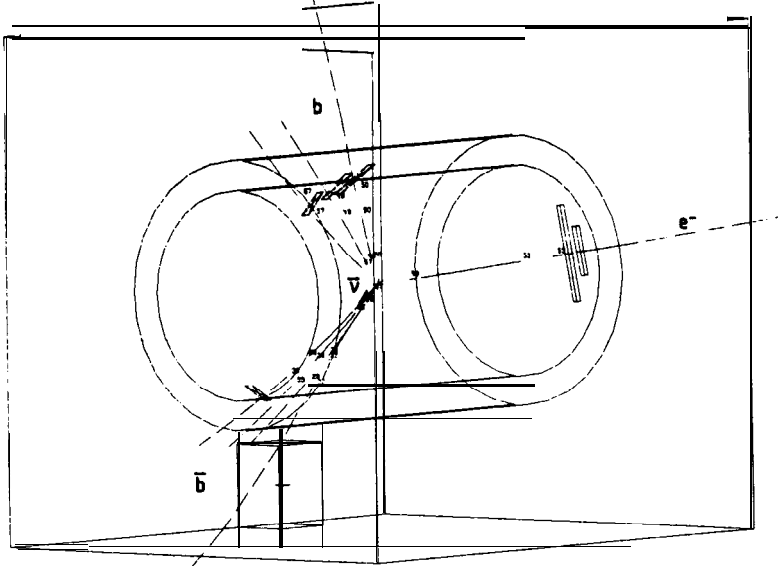


Fig. 22d.

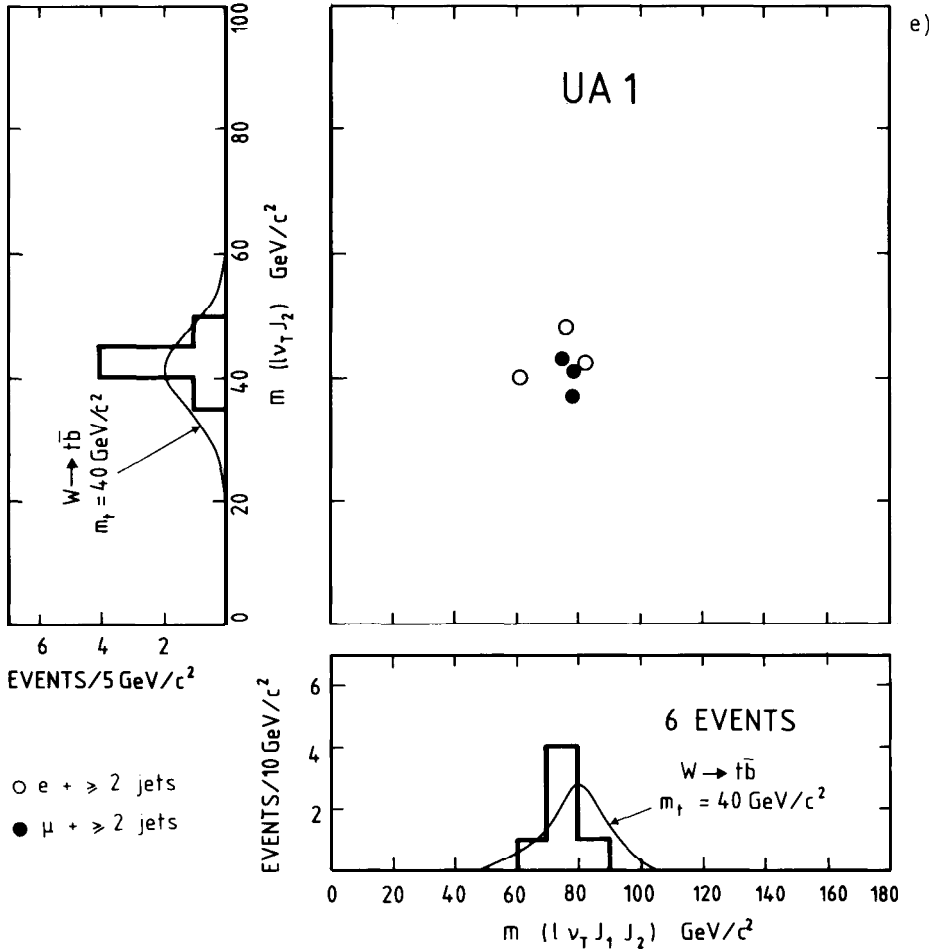


Fig. 22e.

that we now searched for electron and muon pairs rather than for electron-neutrino coincidence. The process is then

$$\bar{p}+p \rightarrow Z^0+X, \quad Z^0 \rightarrow e^+e^- \text{ or } \mu^+\mu^-.$$

This reaction is approximately a factor of 10 less frequent than the corresponding  $W^+$  leptonic decay channels. A few events of this type were therefore expected in our muon or electron samples. Evidence for the existence of the  $Z^0$  in the range of masses accessible to the UA1 experiment has also been derived from weak-electromagnetic interference experiments at the highest PETRA energies, where deviations from point-like expectations have been reported (Fig. 23).

We first looked at events of the type  $Z^0 \rightarrow e^+e^-$  [25,26]. As in the case of the  $W^+$  search, an electron signature was defined as a localized energy deposition in two contiguous cells of the electromagnetic detectors with  $E_r > 25 \text{ GeV}$ , and a small (or no) energy deposition ( $\leq 800 \text{ MeV}$ ) in the

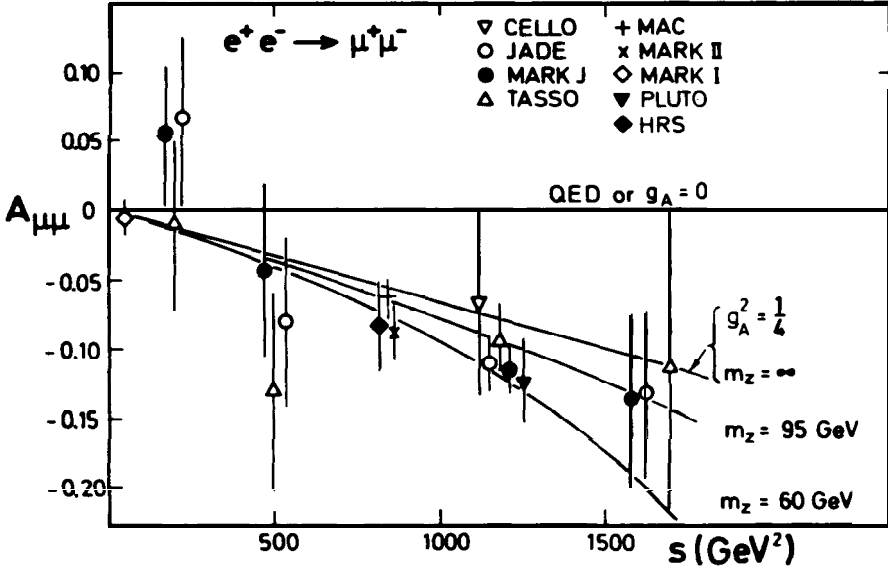


Fig. 23. Experimental evidence for a weak-electromagnetic interference effect in the process  $e^+e^- \rightarrow \mu^+\mu^-$  at high-energy colliding beams. It can be seen that data are better fitted if the presence of a finite mass  $m_z$  propagator is assumed.

hadron calorimeters immediately behind them. The isolation requirement was defined as the absence of charged tracks with momenta adding up to more than 3 GeV/c of transverse momentum and pointing towards the electron cluster cells. The effects of the successive cuts on the invariant electron-electron mass are shown in Fig. 24. Four  $e^+e^-$  events survived cuts, consistent with a common value of  $(e^+e^-)$  invariant mass. One of these events is shown in Figs. 25 and 26. As can be seen from the energy deposition plots (Fig. 27), the dominant feature of the four events is two very prominent electromagnetic energy depositions. All events appear to balance the visible total transverse energy components; namely, there is no evidence for the emission of energetic neutrinos. Except for the one track of event D which travels at less than  $15^\circ$  parallel to the magnetic field, all tracks are shown in Fig. 28, where the momenta measured in the central detector are compared with the energy deposition in the electromagnetic calorimeters. All tracks but one have consistent energy and momentum measurements. The negative track of event C shows a value of  $(9 \pm 1)$  GeV/c, much smaller than the corresponding deposition of  $(49 \pm 2)$  GeV. This event can be interpreted as the likely emission of a hard 'photon' accompanying the electron.

The same features are apparent also from the events in which a pair of muons [27] were emitted. A sharp peak (Fig. 29) is visible for high-mass dimuons. Within the statistical accuracy the events are incompatible with additional neutrino emission. They are all compatible with a common mass value:

$$\langle m_{\mu\mu} \rangle = 85.8_{-5.4}^{+7.0} \text{ GeV}/c^2,$$

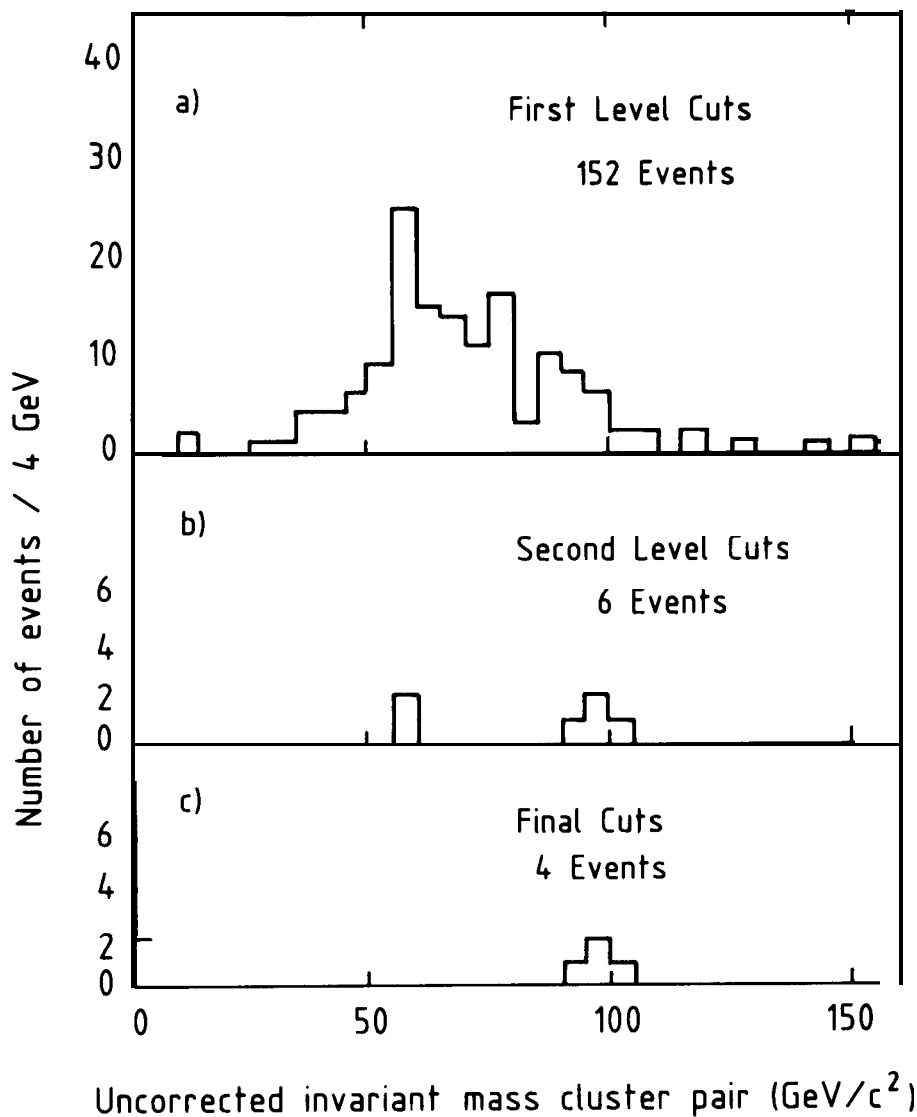


Fig. 24. Invariant mass distribution (uncorrected) of two electromagnetic clusters: a) with  $E_T > 25$  GeV; b) as above, and a track with  $p_T > 7$  GeV/c and projection length of more than 1 cm pointing to the cluster. In addition, a small energy deposition in the hadron calorimeters immediately behind ( $< 0.8$  GeV) ensures the electron signature. Isolation is required with  $\sum p_T < 3$  GeV/c for all other tracks pointing to the cluster. c) The second cluster also has an isolated track.

consistent with the value measured for  $Z^0 \rightarrow e^+e^-$ :

$$\langle m_{ee} \rangle = 95.6 \pm 1.4 (2.9) \text{ GeV}/c^2,$$

where the first error accounts for the statistical error and the second for the uncertainty of the overall energy scale of the calorimeters. The average value for the nine  $Z^0$  events found in the UAl experiment is  $m_{z^0} = 93.9 \pm 2.9 \text{ GeV}/c^2$ , where the error includes systematic uncertainties.

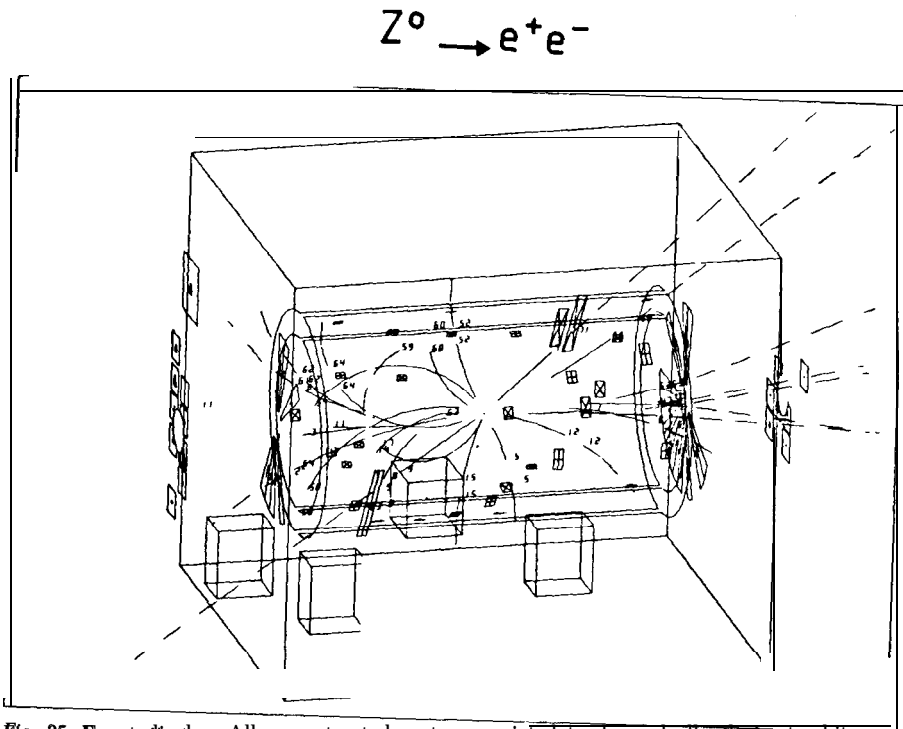


Fig. 25. Event display. All reconstructed vertex-associated tracks and all calorimeter hits are displayed.

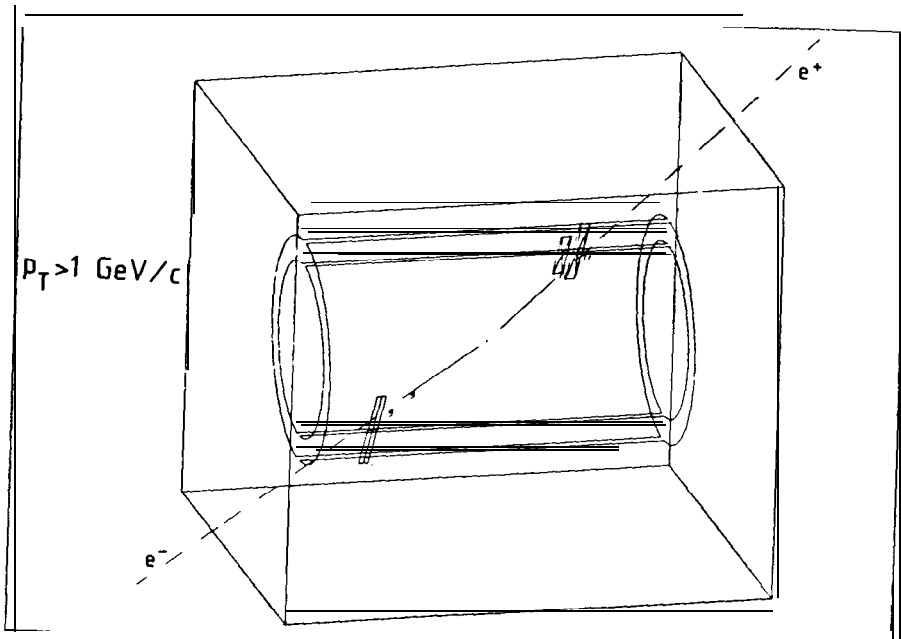


Fig. 26 The same as Fig. 25, but thresholds are raised to  $p_T > 2 \text{ GeV}/c$  for charged tracks and  $E_T > 2 \text{ GeV}$  for calorimeter hits. We remark that only the electron pair survives these mild cuts.

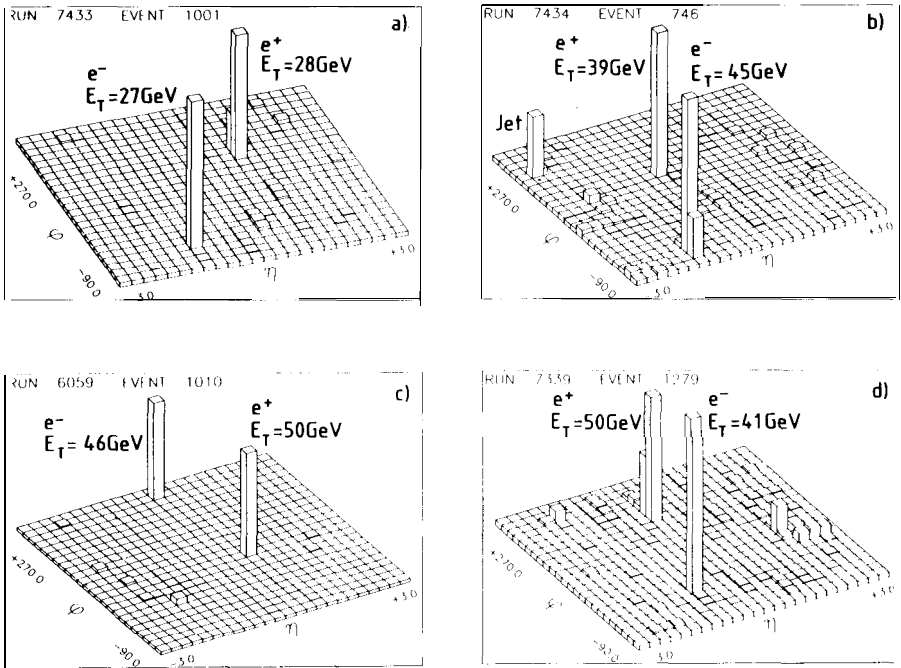


Fig. 27. Electromagnetic energy depositions at angles  $>5^\circ$  with respect to the beam direction for the four electron pairs.

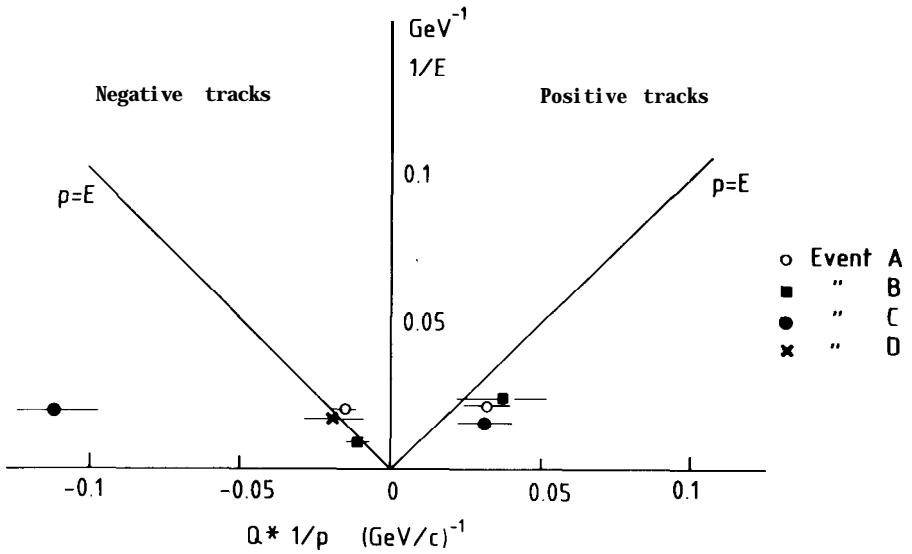


Fig. 28. Magnetic deflection in  $1/p$  units compared with the inverse of the energy deposited in the electromagnetic calorimeters. Ideally, all electrons should lie on the  $1/E = 1/p$  line.

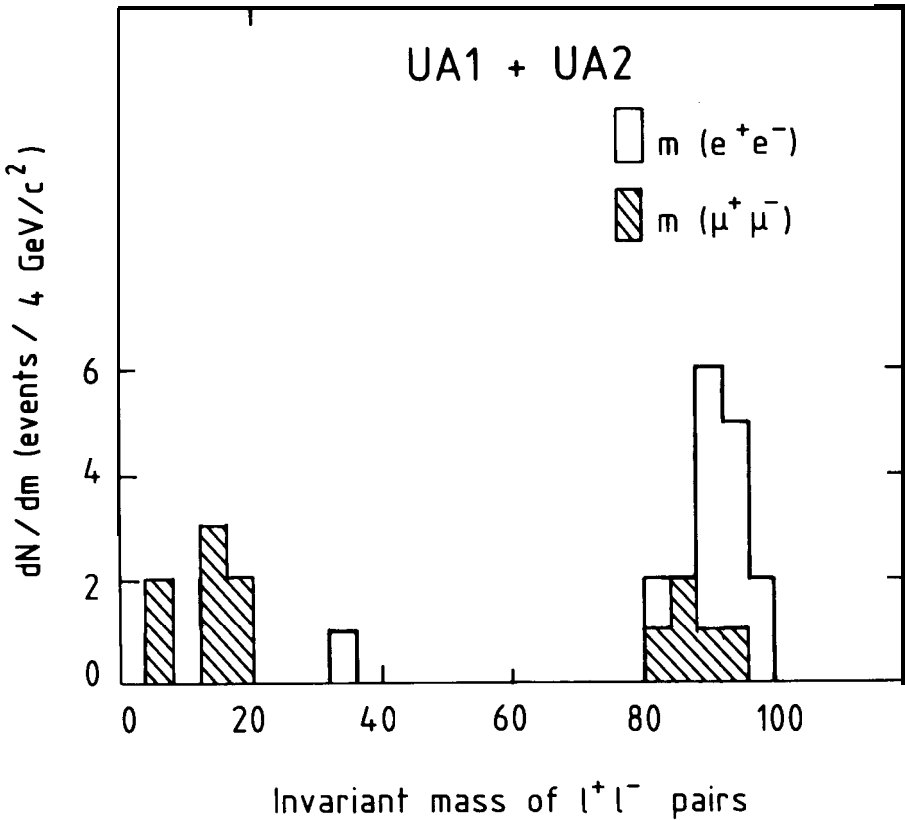


Fig. 29. Invariant mass distribution of dilepton events from UA1 and UA2 experiments. A clear peak is visible at a mass of about 95 GeV/c<sup>2</sup>.

The integrated luminosity for the present data sample is 108 nb<sup>-1</sup>, with an estimated uncertainty of 15 %. With the geometrical acceptance of 0.37, the cross-section, calculated using the four events, is

$$(\sigma \cdot B)_{\mu\mu} = 100 \pm 50 (\pm 15) \text{ pb},$$

where the last error includes the systematics from the acceptance and from the luminosity. This value is in good agreement both with Standard Model predictions [22] and with our results for  $Z^0 + e^+e^-$ , namely  $(\sigma \cdot B)_{ee} = 41 \pm 21 (\pm 7) \text{ pb}$ . From the electron and the muon channels we obtain the average cross-section of

$$(\sigma \cdot B)_{\ell\ell} = 58 \pm 21 (\pm 9) \text{ pb}.$$

### 11. Comparing theory with experiment

The experiments discussed in the previous section have shown that the W particle has most of the properties required in order to be the carrier of weak interactions. The presence of a narrow dilepton peak has been seen around 95 GeV/c<sup>2</sup>. Rates and features of the events are consistent with the hypothesis

Table 2.  $W^\pm$  and  $Z^0$  parameters from the UA1 and UA2 experiments

	UA1	UA2
$N(W \rightarrow e\nu)$	52 <sup>a</sup>	37 <sup>a</sup>
$m_w$ (GeV/c <sup>2</sup> )	80.9±1.5±2.4	83.1±1.9±1.3
$\Gamma_W$ (90 % CL)	≤7 GeV	—
( $\sigma_B$ ) (nb)	0.53±0.08±0.09	0.53±0.10±0.10
$N(W \rightarrow \mu\nu)$	14	—
$m_w$ (GeV/c <sup>2</sup> )	81.0 <sup>a,c</sup>	—
( $\sigma_B$ ) (nb)	0.67±0.17±0.15	—
$N(Z^0 \rightarrow e^+e^-)$	3+1 <sup>c</sup>	7+1 <sup>c</sup>
$m_{z^0}$ (GeV/c <sup>2</sup> )	95.6±1.4±2.9	92.7±1.7±1.4
$\Gamma_{Z^0}$ (90 % CL)	88.5 GeV	86.5 GeV
( $\sigma_B$ ) (nb)	0.05±0.02±0.009	0.11±0.04±0.02
$N(Z^0 \rightarrow \mu^+\mu^-)$	4+1 <sup>c</sup>	—
$m_{z^0}$ (GeV/c <sup>2</sup> )	85.6±6.3	—
( $\sigma_B$ ) (nb)	0.105±0.05±0.15	—
$\sin^2\theta_w = 38.5/m_w$	0.226±0.015	0.216±0.010±0.007
$\rho = [m_w/m_z \cos\theta_w]^2$	0.968±0.045	1.02±0.06

<sup>a</sup>  $p_T^v > 15$  GeV/c

<sup>b</sup>  $p_T^c > 25$  GeV/c

<sup>c</sup>  $Z^0 \rightarrow \ell^+\ell^-\gamma$  ( $E_\gamma > 20$  GeV)

that the neutral partner of the  $W^\pm$  has indeed been observed. At present the statistics are not sufficient to test the form of the interaction experimentally; neither has parity violation been detected. However, the precise values of the masses of  $Z^0$  and  $W^\pm$  now available constitute a critical test of the idea of unification between weak and electromagnetic forces, and in particular of the predictions of the  $SU(2) \times U(1)$  theory of Glashow, Weinberg and Salam [6]. A careful account of systematic errors is needed in order to evaluate an average between the mass determination for the two collider experiments, UA1 and UA2 [28]. Table 2 summarizes all experimental information related to  $W^\pm$  and  $Z^0$ .

The charged vector boson mass is

$$m_{W^\pm} = (80.9 \pm 1.5) \text{ GeV}/c^2 \quad (\text{statistical errors only}),$$

to which a 3 % energy scale uncertainty must be added. In this report a value for the  $Z^0$  mass,  $m_{z^0} = (95.1 \pm 2.5) \text{ GeV}/c^2$ , has been given. Neglecting systematic errors, a mass value is found with somewhat smaller errors:

$$m_{z^0} = (95.6 \pm 1.4) \text{ GeV}/c^2 \quad (\text{statistical errors only}),$$

to which the same scale uncertainty as that for the  $W^\pm$  applies. The quoted errors include: i) the neutral width of the  $Z^0$  peak, which is found to be  $\Gamma < 8.5 \text{ GeV}/c^2$  (90 % confidence level); ii) the experimental resolution of counters; and iii) the r.m.s. spread between calibration constants of individual elements.

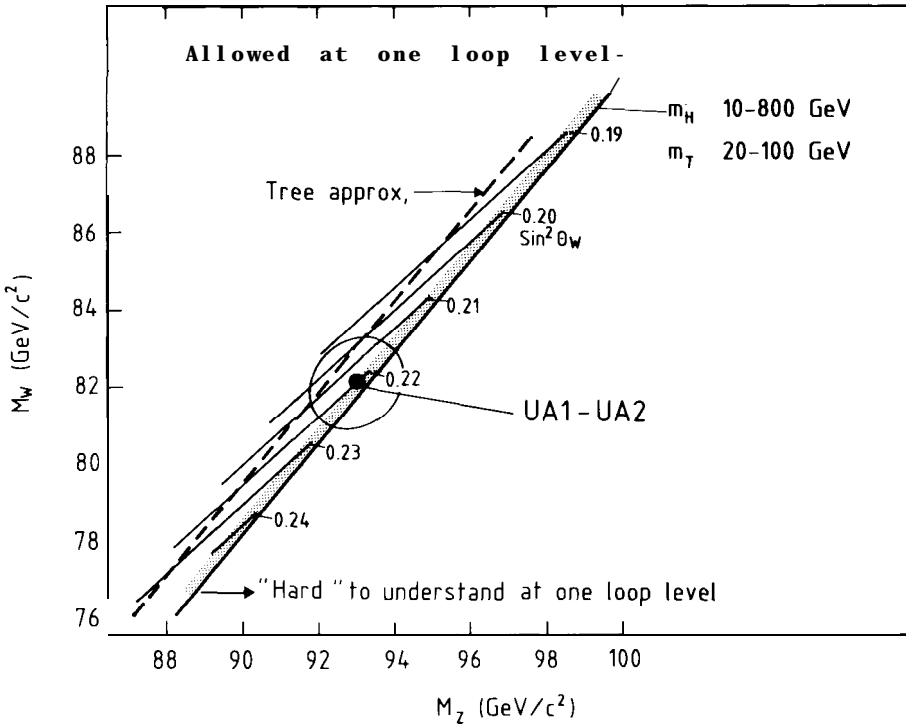


Fig. 30. Comparison between the Standard Model and the experimental results (UA1 and UA2 combined). Theory is from Ref. [29].

It should be remarked that the masses of the IVBs have the following prediction:

$$m_w = [\pi\alpha/\sqrt{2} G_F \sin^2 \theta_W (1-\Delta r)]^{1/2},$$

$$m_Z = m_W / \cos \theta_W,$$

where the value  $\Delta r$  represents the effect of the higher-order radiative corrections, and the second equation can be used as a definition of the Weinberg angle  $\theta_W$ . Since  $G_F$  and  $\alpha$  are known,  $\theta_W$  can be eliminated between equations:

$$m_Z = m_W / (1 - A^2/m_W^2)^{1/2},$$

$$\Delta r = A^2 m_Z^2 / [m_W^2 (m_W + m_Z) (m_Z - m_W)],$$

$$A = (37.2810 \pm 0.0003) \text{ GeV}.$$

Radiative corrections are quite large [29] and detectable at the present level of accuracy. Calculations of order  $O(\alpha) + O(\alpha^2 \ln m)$  give the following result:

$$\Delta r = 0.0696 \pm 0.0020,$$

which is insensitive to the parameters

$$\sin^2\theta_W = 0.217,$$

$$m_t = 40 \text{ GeV}/c^2, \quad m_b = 5 \text{ GeV}/c^2.$$

The main effect can be understood as  $\alpha$  being a running coupling constant, namely:

$$\begin{aligned} a &= 1/137.035962, & \text{at } q^2 = 0, \\ a &= 1/137.5, & \text{at } q^2 = m_W^2. \end{aligned}$$

In Fig. 30 we have plotted  $m_z$  against  $m_w$ . The elliptical shape of the errors reflects the uncertainty in the energy scale. It can be seen that there is excellent agreement with the expectations of the SU(2)xU(1) Standard Model [29].

We can then extract the renormalized value of  $\sin^2\theta_W$  at mass scale  $m_w$ . Inserting the value of  $m_w$  one finds

$$\sin^2\theta_W = 0.220 \pm 0.009,$$

In excellent agreement with the renormalized value of  $\sin^2\theta_W = 0.215 \pm 0.014$  deduced from neutral-current experiments. Using the information of the  $Z^0$  mass, one can determine the parameter  $\varrho$ , related immediately to the isospin of the Higgs particle:

$$\varrho = m_W^2/m_{Z^0}^2 \cos^2\theta_W.$$

Using the experimental values, one finds

$$\varrho = 1.000 \pm 0.036,$$

in perfect agreement with the prediction of  $\varrho = 1$  for a Higgs doublet. Let us point out that  $\varrho$  deviates from 1 at most by 3%, owing to radiative corrections involving possible new fermion generations. The present value seems to indicate no such new fermion families.

We conclude that, within errors, the observed experimental values are completely compatible with the SU(2)xU(1) model, thus supporting the hypothesis of a unified electroweak interaction.

#### ACKNOWLEDGEMENTS

This lecture is based on the work of the UAI Collaboration team, and I would like to express my appreciation of their remarkable achievements which have led to so many exciting results. At present the following persons are members of the collaboration: G. Arnison, A. Astbury, B. Aubert, C. Bacci, A. Bezaguet, R. K. Bock, T. J. V. Bowcock, M. Calvetti, P. Catz, P. Cennini, S. Centro, F. Ceradini, S. Cittolin, D. Cline, C. Cochet, J. Colas, M. Corden, D. Dallman,

D. Dau, M. DeBeer, M. Della Negra, M. Demoulin, D. Denegri, A. Diciaccio, D. DiBitonto, L. Dobrzynski, J. D. Dowell, K. Eggert, E. Eisenhandler, N. Ellis, P. Erhard, H. Faissner, M. Fincke, G. Fontaine, R. Frey, R. Frühwirth, J. Garvey, S. Geer, C. Ghesquiere, P. Ghez, K. L. Giboni, W. R. Gibson, Y. Giraud-Heraud, A. Givernaud, A. Gonidec, G. Grayer, T. Hansl-Kozanecka, W. J. Haynes, L. O. Hertzberger, C. Hodges, D. Hoffmann, H. Hoffmann, D. J. Holthuizen, R. J. Homer, A. Honma, W. Jank, G. Jorat, P. I. P. Kalmus, V. Karimaki, R. Keeler, I. Kenyon, A. Kernan, R. Kinnunen, W. Kozanecki, D. Kryn, F. Lacava, J. P. Laugier, J. P. Lees, H. Lehmann, R. Leuchs, A. Leveque, D. Linglin, E. Locci, J. J. Malosse, T. Markiewicz, G. Maurin, T. McMahon, J. P. Mendiburu, M. N. Minard, M. Mohammadi, M. Moricca, K. Morgan, H. Muirhead, F. Muller, A. K. Nandi, L. Naumann, A. Norton, A. Orkin-Lecourtois, L. Paoluzi, F. Pauss, G. Piano Mortari, E. Pietarinen, M. Pimiä, J. P. Porte, E. Radermacher, J. Ransdell, H. Reithler, J. P. Revo1, J. Rich, M. Rijssenbeek, C. Roberts, J. Rohlf, P. Rossi, C. Rubbia, B. Sadoulet, G. Sajot, G. Salvi, G. Salvini, J. Sass, J. Soudraix, A. Savoy-Navarro, D. Schinzel, W. Scott, T. P. Shah, D. Smith, M. Spiro, J. Strauss, J. Streets, K. Sumorok, F. Szoncsó, C. Tao, G. Thompson, J. Timmer, E. Tscheslog, J. Tuominiemi, B. Van Eijk, J. P. Vialle, J. Vrana, V. Vuillemin, H. D. Wahl, P. Watkins, J. Wilson, R. Wilson, C. E. Wulz, Y. G. Xie, M. Yvert and E. Zurfluh.

## REFERENCES

1. E. Fermi, Ric. Sci. 4 (2), 491 (1933), reprinted *in* E. Fermi, Collected Papers (eds. E. Segré et al.) (University of Chicago Press, Chicago, Ill., 1962), Vol. 1, p. 538; Z. Phys. 88, 161 (1934); English translation: F. L. Wilson, Am. J. Phys. 36 1150 (1968).
2. M. Gell-Mann and M. Levy, Nuovo Cimento 16, 705 (1960).
3. N. Cabibbo, Phys. Rev. Lett. 10, 531 (1963).  
M. Kobayashi and K. Maskawa, Progr. Theor. Phys. 49, 652 (1973).
4. S. S. Gershtein and J. R. Zeldovich, Z. Eksp. Teor. Fiz. 29, 698 (1955).  
R. P. Feynman and M. Gell-Mann, Phys. Rev. 109, 193 (1958).  
E. C. G. Sudarshan and R. E. Marshak, Phys. Rev. 109, 1860 (1958).  
J. J. Sakurai, Nuovo Cimento 7, 649 (1958).
5. O. Klein, in Proc. Symp. on Les Nouvelles Theories de la Physique, Warsaw, 1938 (Institut International de Coopération Intellectuelle, Paris, 1939), p.6.  
O. Klein, Nature 161, 897 (1948).
6. S. L. Glashow, Nucl. Phys. 22, 579 (1961).  
S. Weinberg, Phys. Rev. Lett. 29, 1264 (1967).  
A. Salam, Proc. 8th Nobel Symposium (ed. N. Svartholm) (Almqvist and Wiksell, Stockholm, 1968), p. 367.
7. T. D. Lee and C. N. Yang, Phys. Rev. 119, 1410 (1960).
8. The first realistic scheme for colliding beams was discussed by D. W. Kerst et al., Phys. Rev. 202, 590 (1956). The first suggestion for proton-antiproton intersecting beams was given by G. I. Budker, Proc. Int. Symp. on Electron and Positron Storage Rings, Saclay, 1966 (eds. H. Zyngier and E. Crémieu-Alcan) (PUF, Paris, 1966), p. II-1-1. G. I. Budker, At. Energ. 22, 346 (1967).
9. C. Rubbia, P. McIntyre and D. Cline, Proc. Int. Neutrino Conf., Aachen, 1976 (eds. H. Faissner, H. Reithler and P. Zerwas) (Vieweg, Braunschweig, 1977), p. 683.
10. The 300 GeV programme, CERN/1050 (14 January 1972).

11. S. van der Meer, Internal Report CERN ISR-PO/72-31 (1972).  
D. Möhl, G. Petrucci, L. Thorndahl and S. van der Meer, Phys. Rep. 58, 73 (1980).
12. Design study of intersecting storage rings (ISR) for the CERN Proton Synchrotron, CERN AR/Int. SG/64-9 (1964).
13. A. Astbury et al., A 4x solid-angle detector for the SPS used as a proton-antiproton collider at a centre-of-mass energy of 540 GeV, Proposal, CERN-SPSC 78-6/P92 (1978).
14. The UA1 Collaboration is preparing a large and comprehensive report on the detector (1984). For details see:  
M. Barranco Luque et al., Nucl. Instrum. Methods 176, 175 (1980).  
M. Calvetti et al., Nucl. Instrum. Methods 176, 255 (1980).  
M. Calvetti et al., Proc. Int. Conf. on Instrumentation for Colliding Beam Physics, Stanford, 1982 (SLAC-250, Stanford, 1982), p. 16.  
M. Calvetti et al., IEEE Trans. Nucl. Sci. NS-30, 71 (1983).  
J. Timmer, The UA1 detector, Antiproton proton physics and the W discovery, presented at the 3rd Moriond Workshop, La Plagne, France, March 1983 (Ed. Tran Thanh Van) (Editions Frontières, Gif-sur-Yvette, France), p. 593.  
E. Locci, Thèse de doctorat ès sciences, Paris, 1984, unpublished.  
M. J. Corden et al., Phys. Scr. 25, 5 and 11 (1982).  
M. J. Corden et al., Rutherford preprint RL-83-116 (1983).  
K. Eggert et al., Nucl. Instrum. Methods 176, 217 (1980).  
J. C. Santiard, CERN EP Internal Report 80-04 (1980).  
K. Eggert et al., Nucl. Instrum. Methods **176**, 223 (1980) and 188, 463 (1981).  
G. Arnison et al., Phys. Lett. **121B** 77 (1983).  
G. Arnison et al., Phys. Lett. **128B** 336 (1983).  
The UA2 Collaboration have described their detector, which however makes a more limited use of the missing-energy concept, in Proc. 2<sup>nd</sup> Int. Conf. on Physics in Collisions, Stockholm, 1982 (Plenum Press, New York, 1983), p. 67.  
A. G. Clark, Proc. Int. Conf. on Instrumentation for Colliding Beam Physics, Stanford, 1982 (SLAG-250, Stanford, 1982), p. 169.  
B. Mansoulié, The UA2 apparatus at the CERN  $p\bar{p}$  Collider, Antiproton proton physics and the W discovery, presented at the 3rd Moriond Workshop, La Plagne, France, March 1983 (Ed. Tran Thanh Van) (Editions Frontières, Gif-sur-Yvette, France), p. 609.
15. G. Arnison et al., Phys. Lett. **122B**, 103 (1983).
16. M. Banner et al., Phys. Lett. **122B**, 476 (1983).
17. G. Arnison et al., Phys. Lett. **129B**, 273 (1983).  
C. Rubbia, Proc. Int. Europhysics Conf. on High-Energy Physics, Brighton, 1983 (eds. J. Guy and C. Costain) (Rutherford Appleton Lab., Didcot, 1983), p. 860.
18. G. Arnison et al., Phys. Lett. **139B**, 115 (1984).
19. C. Rubbia, Physics results of the UA1 Collaboration at the CERN proton-antiproton collider, Proc. Int. Conf. on Neutrino Physics and Astrophysics, Dortmund, 1984 (ed. K. Kleinknecht), p. 1.
20. J. F. Owens and E. Reya, Phys. Rev. **D17**, 3003 (1978).  
F. Halzen and W. Scott, Phys. Lett. 78B, 318 (1978).  
F. Halzen, A. D. Martin and D. M. Scott, Phys. Rev. **D25**, 754 (1982).  
P. Aurenche and R. Kinnunen, Annecy preprint LAPP-TH-78 (1983).  
A. Nakamura, G. Pancheri and Y. Srivastava, Frascati preprint LNF-83-44 (1983).
21. G. Altarelli, R. K. Ellis, M. Greco and G. Martinelli, Nucl. Phys. **B246**, 12 (1984).  
G. Altarelli, G. Parisi and R. Petronzio, Phys. Lett. **76B**, 351 and 356 (1978).
22. F. E. Paige, in Proc. Topical Workshop on the Production of New Particles in Super High Energy Collisions, Madison, 1979 (eds. V. Barger and F. Halzen) (AIP, New York, 1979).  
F. E. Paige and S. D. Protopopescu, ISAJET program, BNL 29777 (1981).  
G. Altarelli, R. K. Ellis and G. Martinelli, Nucl. Phys. **B143**, 521 (1978); (E) **B196**, 544 (1978); **B157**, 461 (1979).  
J. Kubar-Andre and F. E. Paige, Phys. Rev. **D19**, 221 (1979).

23. M. Jacob, *Nuovo Cimento* 9, 826 (1958).  
M. Jacob, unpublished (see, for instance, in C. Rubbia, Proc. 9<sup>th</sup> Topical Conf. on Particle Physics, Honolulu, 1983).
24. G. Arnison et al., *Phys. Lett.* **147B**, 493 (1984).
25. G. Arnison et al., *Phys. Lett.* **126B**, 398 (1983).
26. P. Bagnaia et al., *Phys. Lett.* **229B**, 150 (1983).
27. G. Arnison et al., *Phys. Lett.* **147B**, 241 (1984).
28. C. Rubbia, Proc. Int. Europhysics Conf. on High-Energy Physics, Brighton, 1983 (eds. J. Guy and C. Costain) (Rutherford Appleton Lab., Didcot, 1983), p. 860.
29. M. Consoli, Proc. Third Topical Workshop on  $p\bar{p}$  Collider Physics, Rome, 1983 (eds. C. Bacci and G. Salvini) (CERN 83-04, Geneva, 1983), p. 478.  
M. Consoli, S. L. Presti and L. Maiani, Univ. Catania preprint PP/738-14/1/1983.  
M. Veltman, Proc. Int. Europhysics Conf. on High-Energy Physics, Brighton, 1983 (eds. J. Guy and C. Costain) (Rutherford Appleton Lab., Didcot, 1983), p. 880.  
W. Marciano, BNL preprint 33819 (1983).